POLYTECHNIC OF TURIN

Master's Degree Course in Aerospace Engineering

Master's Degree Thesis

Cross-calibration of millimeter spaceborne radars through orbital intersections

Supervisors
Prof. Alessandro BATTAGLIA
Prof. Fabrizio STESINA

Candidate
Filippo Emilio SCARSI

July 2022

Ringrazio la mia famiglia e ringrazio Nicole,
che mi ha supportato durante questo percorso.
Ringrazio anche il professore Alessandro Battaglia,
il mio relatore, per avermi fatto da guida durante
il lavoro e la stesura della tesi di laurea.

Abstract

Spaceborne weather radars provides unique observation of clouds and precipitations, especially in remote areas of the planet, being are an essential tool for the understanding of the Earth's energy and water cycles. A better understanding of those phenomena will increase our skills in weather forecasts and in predicting where an when extreme weather events occur, helping us reducing disaster risk. In fact, as reported by the Weather Meteorological Organization, weather extremes causes recurring damage, loss of life, and economic loss. The necessity of enhancing our capabilities in this area, pushed towards the development of rapidly conically scanning millimeter atmospheric radar systems, such as the Ka-band radars carried by the Tomorrow.io constellation and the WIVERN (WInd VElocity Radar Nephoscope) W-band radar. The advantages brought by this type of radar include the ability of sampling large domains, reducing the clutter and providing measurements of horizontal winds. Traditional calibration methods, e.g. pointing at sea surface at about 12° incidence angle, are not viable for such systems. Therefore, new calibration methodologies are urgently needed.

This dissertation demonstrate the effectiveness of calibrating spaceborne conically scanning radars using cross-calibration, with properly calibrated spaceborne radars working at the same band and orbiting around Earth in the same period of time used as reference.

Cross-calibration can be achieved whether the radar that needs to be calibrated and the radar used as reference illuminate the same calibration target, therefore, if, and when, their footprints intersect. Different pairs of radar systems have been analyzed in this thesis such as the Ka-band Tomorrow.io radar that uses GPM KaPR as the calibrator and Wivern W-band radar that exploits the radars of NASA AOS mission as reference for the calibration. Ice clouds at low temperature are selected to be natural targets for the calibration due to their low proneness to appreciable attenuation.

The orbits of satellites have been propagated and the positions of the radar antenna boresight have been computed based on the orbits propagation. Thus, the radars' ground-track intersections have been determined for different intersection criteria defined by cross-over within a certain time and within a given distance. The climatology of calibrating clouds has been studied using the CloudSat CPR and GPM KaPR dataset for the W and the Ka-band, respectively, in order to find how those clouds are distributed on the globe and at what frequency they occur. Then the global distribution of radar cross-overs and the climatology of clouds have been merged in order to obtain how many calibration points are collected by the radars involved in the cross-calibration.

The CloudSat and GPM datasets have been further exploited to analyze the statistical correlation between the reflectivity probability distribution function of the calibrating clouds for different distance at which the clouds are sampled, in order to find the optimal intersection criterion that optimizes the calibration accuracy and minimizes the time needed to achieve it.

The results demonstrate the feasibility of cross-calibrating a Ka and a W-band conically scanning radar, e.g. the ones carried by the Tomorrow.io constellation and Wivern, within 1 dB every few days and every week, respectively. An even better calibration within 0.5 dB can be achieved every week for the Tomorrow.io radars, while, the less accurate, but quicker, calibration of 2 dB is established within less than a day (Tomorrow.io) and every few days (Wivern). These results meet the mission requirements and the standards in accuracy currently achieved with conventional calibration techniques.

Table of Contents

List of Tables

List of Figures

Chapter 1

Introduction

The understanding of the Earth's water and energy cycles and their interconnection is one of the big challenges that the international scientific community has to face in the next years. In fact, three out of seven of the "Grand challenges" promoted by the World Climate Research Program involves this topic; they are:

1. Clouds, Circulation and Climate sensitivity;

2. Understanding and predict Weather and Climate Extremes;

3. Water for the Food Baskets in the World.[21, 6]

In fact, as reported by the World Metereological Organization (WMO), extreme weather events, which are increasing in magnitude and frequency due to the warming climate, cause recurring damage, economic loss and loss of life, with windstorms being the biggest contributors to these weather related hazards [20, 13] .
These challenges requires an improvement in our skill of observing and predicting when, where, and why clouds forms, whether they generate precipitation or not, and how much precipitation they produce, both in the current and warming climate [6].
Clouds and precipitation are central elements in the Earth's energy and water cycles. Clouds play a relevant role in the Earth's radiation budget through the absorption, reflection and emission of radiation, and through the vertical realising of latent heat. They are also fundamental in the hydrological cycle by redistributing moisture and generating precipitation. Precipitation affects the Earth's energy budget: at the global scale, the annual mean precipitation is equivalent to the mean evaporation. The latent heat required to evaporate water at the ocean surfaces is transported upwards and then released in the atmosphere when condensation occurs in correspondence to cloud formation. Precipitation also shapes the ecological system, drives freshwater resources and produces important impact over urban and

coastal regions, especially during extreme weather events such as hurricanes, floods and drought [6].

Spaceborne atmospheric radars are a fundamental tool for the observation of clouds, precipitations and winds, especially on the ocean and in remote areas of the planet. They help to increase our knowledge in the Earth's energy and water cycles and in all those phenomena related to it, to improve our weather prediction skills and to predict when and where extreme weather events occur in order to decrease disaster risk. The efforts of the scientific community are aimed at filling the gaps in spaceborne weather radars capabilities [6].

The first satellite-based cloud and precipitation measurements were carried out by passive infrared sensors but they were only sensing the upper layers of the atmosphere. In fact the infrared radiation, unlikely the microwave, cannot penetrate clouds and precipitations. Active microwave sensors were deployed in order to meet the need of having detailed measurements on the vertical structure of these phenomena. Today, radar operating at the millimeter wavelengths (such as Ka-band and W-band, see [11] for nomenclature), also called "cloud radars", are one of the principal instruments used for the observation of clouds, due to their sensitivity to small ice crystals and cloud droplets. The W-band spaceborne radars, that had the first entry in space with the launch of CloudSat CPR, filled a gap between the cloud and the precipitation radars, being able to adequately detect both phenomena [6].

The need of facing all those challenge previously described, such as the mitigation of the impact of severe weather events, have given a push towards Earth observation missions involving rapidly conically scanning millimeter radars. For example, Tomorrow.io is a US private company that is currently developing a constellation of small Ka-band (35 GHz) wide-swath conically and cross-track scanning radars with the goal of giving global coverage of precipitation with a temporal resolution adequate for the actuation of operations aimed at reducing the damage cause by weather extremes. Also, a W-band (94 GHz) conically scanning radar focusing in providing in-cloud winds for improving numerical weather prediction is undergoing the ESA Earth Explorer 11 selection program Phase 0 studies as part of the Wivern mission[2, 3, 13, 14]. In figure Fig. 1.1 is shown the geometry of the Wivern radar scanning as an example of conical scanning.
The advantages brought by the conical scanning include the capability of easily sample large domains, reducing the effect of the clutter and providing measurements of horizontal winds [17]. However, the external reflectivity calibration of such radars cannot be achieved using the standard external calibration technique used for the other atmospheric radars, as, for example, for CloudSat CPR [24] or for the GPM radars [16]. Therefore, the development of a new calibration procedure viable for this new type of radars is necessary. In fact, reflectivity radar calibration is essential to provide realistic quantitative estimation of precipitation and mass contents.

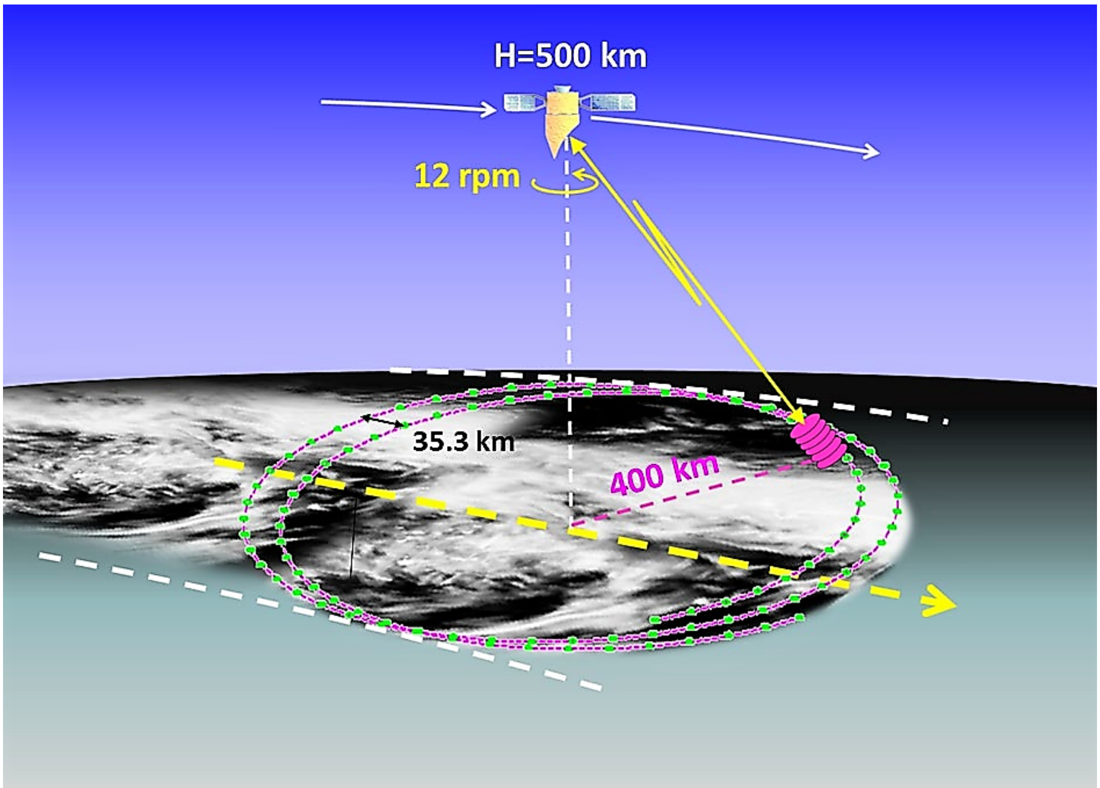

Figure 1.1: Example of a conical scanning. The radar shown in the figure is the Wind Velocity Radar Nephoscope (WIVERN). Figure extracted from [3].

This dissertation investigates a new methodology for the calibration of millimeter conically scanning spaceborne radars via cross-calibration with in-orbit reference systems by using clouds ("natural targets") that have similar reflectivities when seen from different viewing directions. By combining orbit calculation and climatological analysis of the calibrating targets it discusses whether this new methodology is feasible or not and what is the calibration accuracy achievable with this technique. The thesis describes in detail a general strategy to implement the cross-calibration process, to evaluate its effectiveness and the time needed to calibrate the radar within a certain accuracy. This work, now submitted as a journal paper [4], will be of paramount importance for monitoring the calibration of upcoming missions involving conically scanning cloud radars.

Chapter 2

Radar theory and radar calibration techniques

Radar (RAdio Detection And Ranging) is an instrument that emits a strong signal at radio or microwave frequencies and capture the echoes that occur if the signal is reflected from objects known as targets. Since the instrument provides the energy needed itself, i.e. it is categorized as an active remote sensor, what is transmitted is well known and more information can be retrieved than if a passive remote sensor is used, such as the time elapsed between the transmission for the signal and the reception of the echo, how strong is the captured echo respect to the transmitted signal and how the frequency and polarization of the signal changed. The steps that describe how a radar works can be summarized as follow:

1. The radar transmitter generates a strong microwave signal;
2. the antenna focuses the signal towards a specific direction in order to get information from targets at a given location.
3. the radar receiver with the help of a receiving antenna acquires the faint echoes from the targets. The intensity of the returned signal is a very little fraction of what is emitted.
4. Signal processor extracts as much raw data as possible from the received signal.
5. The raw data are processed in order to get meteorological information. [11]

Weather radars operates at defined ranges of frequency. The operational bands are those who belongs to the part of the EM spectrum called "atmospheric windows" because the atmosphere is transparent at those frequencies and causes minimal attenuation to the signal. In Fig. 2.1 is shown how signal attenuation varies with the frequency; it can be notice that some local maxima and minima exists and the radar bands correspond to the values of those frequency where local minima of attenuation are present.

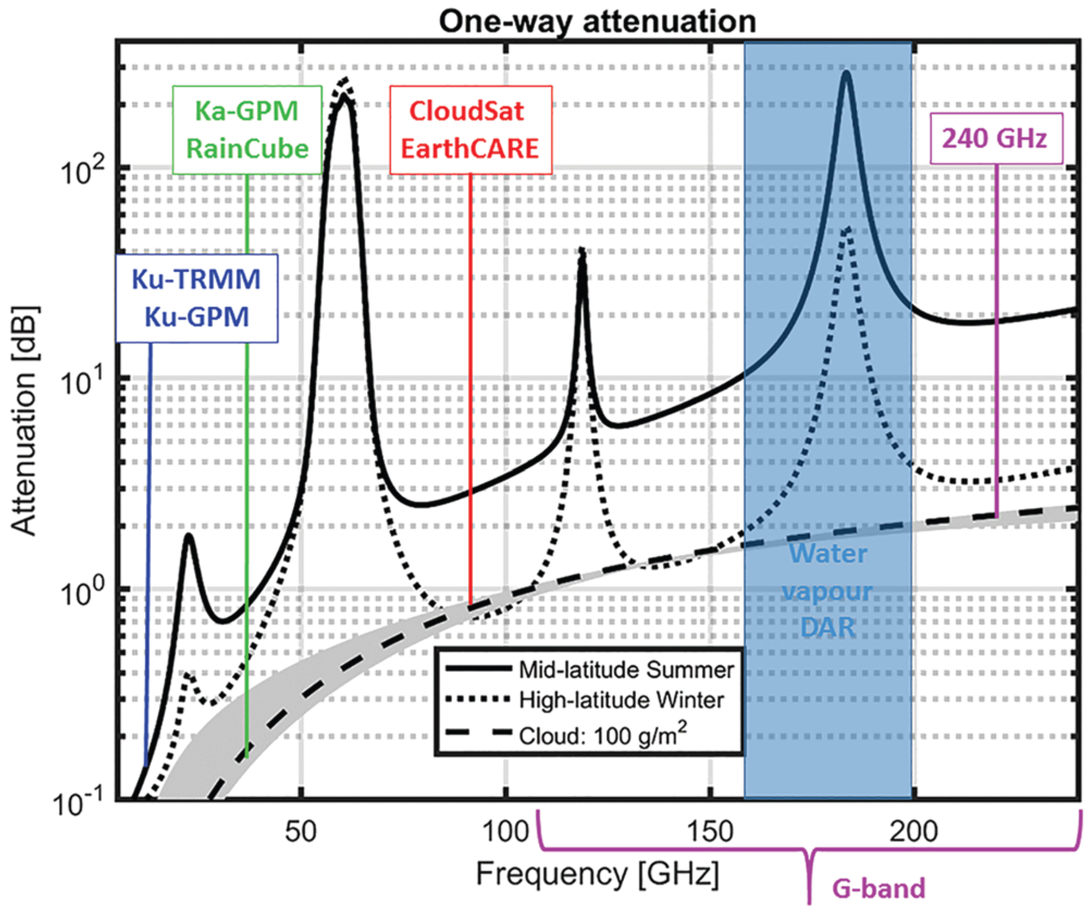

Figure 2.1: Gas attenuation in the range of frequencies between 5 and 250 GHz for two types of atmospheres (a very moist, mid-latitude summer atmosphere and a very dry, high-latitude winter atmosphere). Attenuation due to cloud water at 10°C for a total of 100 g/m2 is plotted in dashed line with the gray shading corresponding to the variability when moving temperature from -35°C to +30°C. Radar frequencies are generally selected in the window regions, that is, away from the water vapor and the oxygen absorption bands, apart for the differential absorption radar (DAR) with frequency located in the 183 GHz water vapor absorption band (blue shaded region). Allocation of current and planned spaceborne radar systems is shown as well. Figure extracted from [6].

While an electromagnetic (EM) wave travels through the atmosphere, it can encounter objects or particles that absorb and reflects portion of the incident EM wave. This phenomenon is known as scattering and exists in different regimes, depending on the EM wavelength, λ, and on the scatterer size. If the particle dimension is smaller than λ, the Rayleigh scattering occurs. In this regime, the fraction of scattered radiation is proportional to D^6/λ^4, where D is the diameter of the scatterer, assuming it is spherical. Therefore, given a scatterer particle diameter D, the scattered radiation increases if λ decreases. Fixed a radiation wavelength λ, smaller particles produce less scattering than bigger ones. Hence, smaller particles are easier to detect by shorter wavelength radars.[11]

Since most of the components of clouds and precipitations are much smaller than the usual wavelengths employed in radars, they behave as Rayleigh scatterers. For such targets, a quantity called the radar reflectivity factor per unit volume, Z, can be defines as

$$Z = \int_0^\infty N(D) D^6 dD \tag{2.1}$$

where $N(D)$ is the number of hydrometeors of diameters D per unit volume, D is expressed in millimeters and Z in $mm^6 m^{-3}$. Since the magnitude of particles diameter can vary of many orders of magnitude, it can be convenient to express the reflectivity factor in decibel of $mm^6 m^{-3}$ as

$$Z_{dBZ} = 10 \log_{10} Z. \tag{2.2}$$

Z can also be expressed as

$$Z = \eta \frac{\lambda^4 10^{18}}{\pi^5 |K|^2} \tag{2.3}$$

where λ is the wavelength, $\|K\|$ is the dielectric constant of the scatterers and η is the radar reflectivity. [11]

The radar reflectivity η can be obtained from the radar range equation

$$P_{rec} = \frac{P_t \lambda^2 G_{rec} G^2 \Omega \Delta \eta}{(4\pi)^3 r^2 L_a} = \frac{P_t \eta}{C r^2 L_a} = \mathcal{C} \frac{\eta}{r^2} \tag{2.4}$$

where P_{rec} is the output power for the receiver, P_t is the transmitted power, G_{rec} is the receiver gain, G is the antenna gain, r is the range to the atmospheric target, Ω is the integral of the normalized two-way antenna pattern, Δ is the integral of the received waveform shape (proportional to the pulse-length $c_0\tau/2$), and L_a is two-way atmospheric loss and C is the radar constant. $\mathcal{C}$ is a term that represents the radar characteristics, the radar transmitted power and the losses. η, and thus Z can be computed from with Eq. 2.3 and by easily rearranging Eq. 2.4. However, since in the most cases the composition of the target is not known, the value of K in uncertain. So, it is more convenient to define an equivalent (attenuated) reflectivity factor, Z_e, computed respect to the dielectric constant of the water at

10°, K_w [24]

$$Z_e = \eta \frac{\lambda^4 10^{18}}{\pi^5 \left|K_w\right|^2} \tag{2.5}$$

The minimum reflectivity factor detectable by the radar receiver, Z_{min}, can be computed substituting Eq. 2.5 in Eq. 2.4 and by assuming all the power output for the receiver is noise ($P_{rec} = P_{noise}$)

$$Z_{min} = \frac{C P_{noise} r^2 L_a \lambda 10^{18}}{P_t \pi^5 \left|K_w\right|^2} \tag{2.6}$$

Z_{min} can be also called single pulse sensitivity of the radar. It can be noticed that, fixed r, higher is λ, and higher is the minimum detectable value of reflectivity, i.e. the sensitivity of CloudSat CPR W-band (94 GHz) radar after integration is -30 dBZ, while that of GPM KaPR Ka-band (35.5 GHz) is +13 dBZ.

2.1 Radar calibration

Radar calibration consists in determining the value of $\mathcal{C}$ of Eq. 2.4, in order to be able to determine a correct estimation of the reflectivity of the target η.

Radar calibration can be realized by simply determine $\mathcal{C}$ from the radar properties provided by its constructor and from an estimation of the losses. However, usually radar's attributes change during the entire life of the radar, e.g. caused by the degradation of some components due to the interaction with the environment. Therefore, this calibration method is not enough accurate and it's better to pair it with other techniques.

External target calibration

External target calibration of a radar system is usually performed by measuring the power backscattered (P_{rec}) from a calibration target of known radar cross section (i.e. reflectivity). Through the substitution of P_{rec} and the already known η into the radar equation (Eq. 2.4), the value of $\mathcal{C}$ is determined (note that the range r is known and, moreover, for spaceborne radars, its value is about the same as the altitude of the satellite and can be precisely retrieved through geometrical considerations [see Section 3.3]).

Traditional passive calibration targets are steel spheres and metal plates. This type of targets are impractical to construct and to use in some application because their dimension must be excessively large in order to have an enough big radar cross section to be detectable against the background. Thus, in some cases, such as for the calibration of GPM DPR [16], an Active Radar Calibrator (ARC) is used in those cases where the traditional passive calibration targets are impractical to be used. It is a ground system composed a receiving and a transmitting antenna and a RF amplifier; it can take a large radar cross section and a broad pattern while maintaining a small dimension [7].

Earths surface can also be used as calibration target. The normalized radar cross section (σ^0) of the Earth's surface, expressed in decibels, is

$$\sigma^0 = \frac{P_{rec}(r\pi)^3 r^2 L_a}{P_t \lambda^2 G_{rec} \Omega} \frac{1}{\cos(\theta)} = \frac{C\Delta}{\cos(\theta)} \frac{P_{rec} r^2 L_a}{P_t} = \frac{1}{\mathcal{C}} \frac{P_{rec} r^2}{\cos(\theta) P_t} \tag{2.7}$$

being θ the incidence angle; at nadir the cosine term can be neglected. At incidence angle close to normal ($0\,°$), σ^0 measured in clear air and over water depends only on wind speed and direction, atmospheric loss (L_a), and, to a lesser extent, on sea surface temperature. While, at incidence angle at approximately $10°$, its dependency on the wind speed and direction is negligible at Ku, Ka and W-band. Therefore the ocean normalized radar cross section at an off-nadir pointing angle equal to $10°$ is almost constant and well known and, through Eq. 2.7, can be used to retrieve the value of $\mathcal{C}$ and calibrate a the radar system. For CloudSat CPR, the values of σ^0 measured pointing at nadir (which is the standard data acquisition mode of this system) were used to monitor the stability of the instrument calibration, While the end to end calibration of the instrument is achieved by steering, once a month, the CPR antenna $10°$ to the left or right of the orbital plane, over cloud free oceanic areas [24, 5, 25].

The external target calibration strategy is non viable for rapidly conically scanning spaceborne radars because of their large and constant off-nadir pointing angle that make the calibration on oceanic surfaces at $10°$ incidence angle impractical.

Cross-calibration

This dissertation presents a new methodology, the cross-calibration, to achieve radar calibration for conically scanning spaceborne radars.

Lets assume we have a pair of two spaceborne radars carried by two satellites orbiting around Earth at the same time. One of them is the radar that needs to be calibrated, like a conically scanning radar. The other is a cross-scanning or non-scanning radar, thus it is well calibrated with the usage of standard methods. If the two radars are pointing at the same target, the well calibrated radar can provide a true reflectivity value of the target, which can be used as reference for the calibration of the other radar. The cross-calibration could happen only if the radars are pointing at the same exact target. However, this conditions are unlikely to happen and it is possible to introduce some criteria, called intersection (or coincidence) criteria, that define what we consider "two radar pointing at the same target". Each intersection criteria is composed by a time, Δt and a distance, Δr, constraint. Given a criterion, if the two radars have a cross-over (we also refers to it as footprint intersection or ground-track intersection) within a certain time and within a certain distance, they are looking at the same target, according to that criterion.

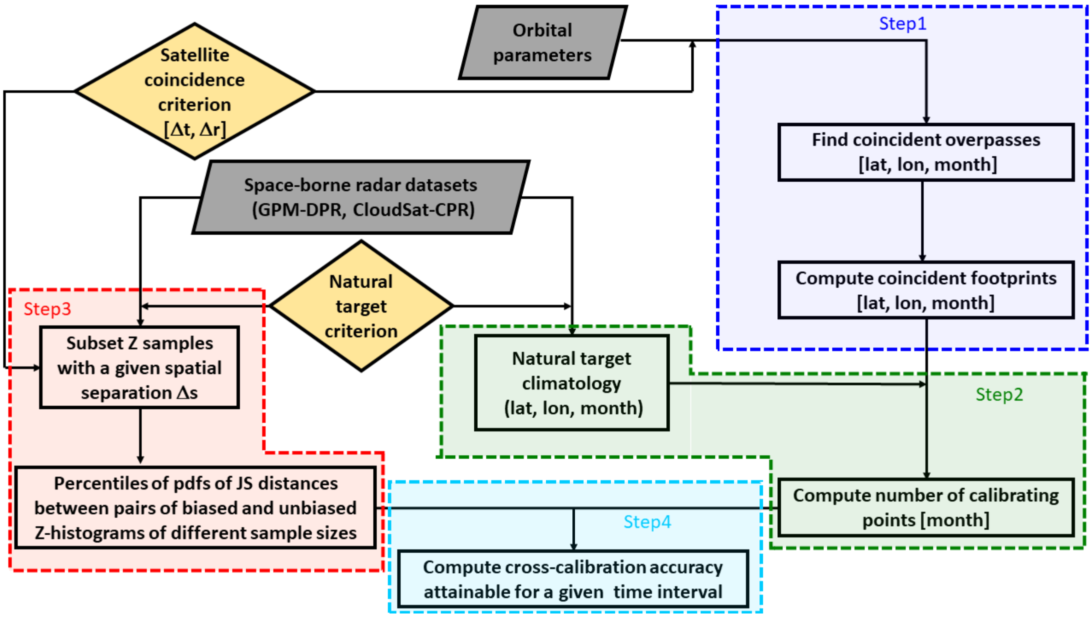

Figure 2.2: A flow-chart illustrating the cross-calibration procedure adopted. Figure submitted in [4].

The procedure adopted for assessing the accuracy of the cross-calibration between two spaceborne radars is composed by four steps

- **Step 1.** Once a coincidence criterion is defined, the orbits of the two satellites are propagated and the observing geometry of the system is used to compute the footprint of the radars. Then the cross-overs between footprints, defined by the coincidence criterion, are computed. The latitude and the longitude of those points are retrieved to geolocate each point. Usually, the global distribution of intersection points is more latitude dependent than longitude dependent.

- **Step 2.** The definition of cross-calibrating targets is established and the climatology of the mean number of layers is computed for each month, based on datasets provided by past or existing mission carrying millimeter radars. The layers's thickness is chosen based on the vertical resolution of the two radars involved in the cross-calibration. Thus, the calibrating layers have been geolocated and their global distribution and the frequency at which they occur are determined. Then, the climatology of calibrating layers is combined with the coincident footprint to obtain the mean number of calibrating points per unit time, e.g. weekly.

- **Step 3.** Past millimeter radar mission datasets can be further exploited in order to produce grouped reflectivity data into sample pairs separated by a given distance, Δs, called separation distance. Δs is chosen based on the coincidence criterion. The probability distribution functions (PDFs) of those reflectivity data are computed and the similarity between PDFs of two sample separated by Δs is determined through the Jensen-Shannon (J-S) distance [10]. A large ensambles of reflectivity PDFs is built in order to find the behaviour and the variability of the J-S distances. This step is necessary to determine what is the statistical noise between two calibrating target sampled at a certain distance from each other. It simulates the cross-calibration process. How some miscalibration bias affects the J-S distances is determined, and consequently, it is possible to asses what is the number of calibrating points necessary to detect that calibration bias.

- **Step 4.** Combining the result of step 2 with those of step 3, for any coincidence criterion, it is possible to evaluate the time needed to collect the number of calibration points necessary to achieve a certain calibration accuracy, and what is the most optimal criterion to adopt in the cross-calibration.

The cross-calibration procedure is described in Fig 2.2.

Chapter 3

Orbit intersections

This chapter provides a detailed description of Step 1. The goal is to compute and geolocate the radar cross-overs starting from the orbital parameters of the satellites' orbit.

Table 3.1: Specifics of the Tomorrow.io and GPM satellites orbits and instruments [18, 19].

Radar		Tomorrow.io1	Tomorrow.io2	GPM KaPR
Orbital element				
Eccentricity	e	0.00125	0	0
Semi-major axis [km]	a	6928	6928	6785
Inclination [deg]	i	97.400	50	65
RAAN [deg]	Ω	-169.3870	0	0
Argument of periapsis [deg]	ω	90	0	0
Mean anomaly [deg]	M	90	0	0
Mean LTAN [hour]		6.000	-	-
Epoch $t0$		2019-01-01, 06:00:00		
Reference Frame		J2000		
Instrument specifics				
RF output frequency		Ka band		
Scanning type		Conical		Cross-track
Swath width [km]		400	400	245
Off-nadir pointing angle [deg]	γ	20°		0-17°
Antenna rotating speed [rpm]		12		-

Tomorrow.io is a mission developed by a US private company that is going to deploy a constellation of satellites carrying a conically scanning Ka-band atmospheric radar. Two types of orbits are considered in this analysis. Both are circular and characterized by an altitude of 500 km. The first has an orbital inclination of 50°. The second is sun-synchronous.

GPM KaPR radar is used as the calibrator. GPM is a NASA mission characterized by a spacecraft located on a circular and 65° inclined orbit and 407km altitude, carrying a cross-track scanning Ka-band radar. Detailed orbital parameters and instrument specifications are listed in table 3.1.

Table 3.2: Specifics of AOS and Wivern satellites orbits and instruments, as proposed in a recent ESA Earth Explorer 11 call for Wivern [14].

Radar		Wivern	AOS1	AOS2
Orbital element				
Eccentricity	e	0.00125	0	0
Semi-major axis [km]	a	6878	6778	6820
Inclination [deg]	i	97.400	50	97.213
RAAN [deg]	Ω	-169.3870	0	122.922
Argument of periapsis [deg]	ω	90	0	0
Mean anomaly [deg]	M	90	0	0
Mean LTAN [hour]		6.000	-	1.500
Epoch $t0$		2019-01-01		
		06:00:00		01:30:00
Reference Frame		J2000		
Instrument specifics				
RF output frequency		W band		
Scanning type		Conical	No scanning	
Swath width [km]		800	-	
Off-nadir pointing angle [deg]	γ	38°	0°	
Antenna rotating speed [rpm]		12	-	

Wivern mission will deploy a satellite to a 500 km altitude and sun-synchronous circular orbit, carrying a conically scanning W-band atmospheric radar.
The reference radars used for the calibration of Wivern are the NASA AOS radars. Two orbits are analyzed, one is a 400 km altitude and 50° inclination orbit, the other is a 450 km altitude sun-synchronous orbit. Both spacecrafts will carry an along-track scanning W-band atmospheric radar.
Detailed orbital parameters and instrument specifications are listed in Tab. 3.2.

We use "A" and "B" to refer to the the radar that needs to be calibrated and to the radar used as reference, respectively. Two cases for both W and Ka-band application are analyzed:

- Wivern (A) – AOS1 (B)
- Wivern (A) – AOS2 (B)
- Tomorrow.io1 (A) – GPM KaPR (B)
- Tomorrow.io2 (A) – GPM KaPR (B)

3.1 Intersection criteria

Table 3.3: Different combinations of temporal and spatial constraints considered in this study that define an "intersection". The third column has been computed by using Eq. 5.1 with $v_{wind} = 20\,\mathrm{ms}^{-1}$ which is a reasonable value for upper level winds.

Criterion #	Time constraint Δt [minutes]	Distance constraint Δr [km]	Δs [km]
1	15	25	30.8
2	15	50	53.1
3	15	100	101.6
4	15	200	200.8
5	15	500	500.3
6	15	1000	1000.2
7	15	2000	2000.1
8	30	25	43.8
9	30	50	61.6
10	30	100	106.3
11	30	200	203.2
12	30	500	501.3
13	30	1000	1000.6
14	30	2000	2000.3
15	45	25	59.5
16	45	50	73.6
17	45	100	113.6
18	45	200	207.2
19	45	500	502.9
20	45	1000	1001.5
21	45	2000	2000.7

In order to calculate the coincidence points, defining what is a coincident overpasses (or intersection) is necessary. An intersection point is a point on the Earth's surface that is illuminated by both radars. Two observations made by different sensors are coincident if they happen withing a certain time interval Δt (time constraint) and within a certain distance Δr (distance constraint). An intersection criterion can be defined by a combination of Δt and Δr. The intersection criteria are reported in Tab. 3.3.

Since natural targets, such as clouds, can change in time and distance, the two instruments would not see the same exact target. Hence, a cloud correlation study is necessary to determine how the number of calibration points and the accuracy of calibration are affected by the distance and the time constraints. This study will be described in the next chapters.

3.2 Orbital mechanics

In this analysis, the orbital problem has been treated as a two-body problem. The mass of the secondary bodies, the spacecrafts, have been considered negligible with respect to the mass of the main body, the Earth.

3.2.1 Coordinate systems

The coordinate systems involved in this chapter are described below. All the coordinate systems here reported are right-handed and orthogonal.

The perifocal reference frame is an inertial coordinate system centered at the focus of the orbit, thus, at the center of the main body (in this case, the Earth). The fundamental plane is the orbital plane. The coordinate system is composed by the unit vectors $\hat{\mathbf{p}}$, $\hat{\mathbf{q}}$ and $\hat{\mathbf{w}}$. The first two lie on the orbital plane. $\hat{\mathbf{p}}$ is directed toward the periapsis and $\hat{\mathbf{q}}$ is rotated by $90\,^{c}irc$ towards the secondary body motion. $\hat{\mathbf{w}}$ is perpendicular to the orbital plane and completes the right-handed reference frame. [1]

The geocentric-equatorial reference frame is an inertial system with its origin at the Earth's center. The fundamental plane is the Earth's equator. The unit vector $\hat{\mathbf{I}}$ points in the direction of the vernal equinox, $\hat{\mathbf{K}}$ points towards the North Pole and $\hat{\mathbf{J}}$ is consequently defined to complete the right-handed reference frame. It is important to notice that, while the Earth rotates around its axis, the geocentric-equatorial reference is non-rotating and remains fixed with respect to the stars (except for the precession of the equinoxes, which is not taken into account in this study). Therefore a relative motion between the Earth and this coordinate system is present.

The Earth-Centered-Earth-Fixed (ECEF) coordinate system has its origin at the Earth's center and its fundamental plane is the Earth's equator. The $\mathbf{Z}$-axis is directed towards the North Pole. Instead, the $\mathbf{X}$-axis, which lies on the fundamental plane, passes through the prime meridian. The ECEF reference frame is fixed to the Earth and rotates with the planet and, therefore, is not an inertial reference frame.

The Local-Vertical Local-Horizontal reference system (depicted in Fig. 3.2) is used to describe the relative motion with respect to the satellite. The center of the spacecraft is the origin of the coordinate system. The $\mathbf{x}$-axis is located on the radial between the Earth's center and the origin of the reference frame pointing outward the radial (local vertical). The $\mathbf{z}$-axis is normal to the orbital plane, while the $\mathbf{y}$-axis points towards the motion of the spacecraft (local horizontal).

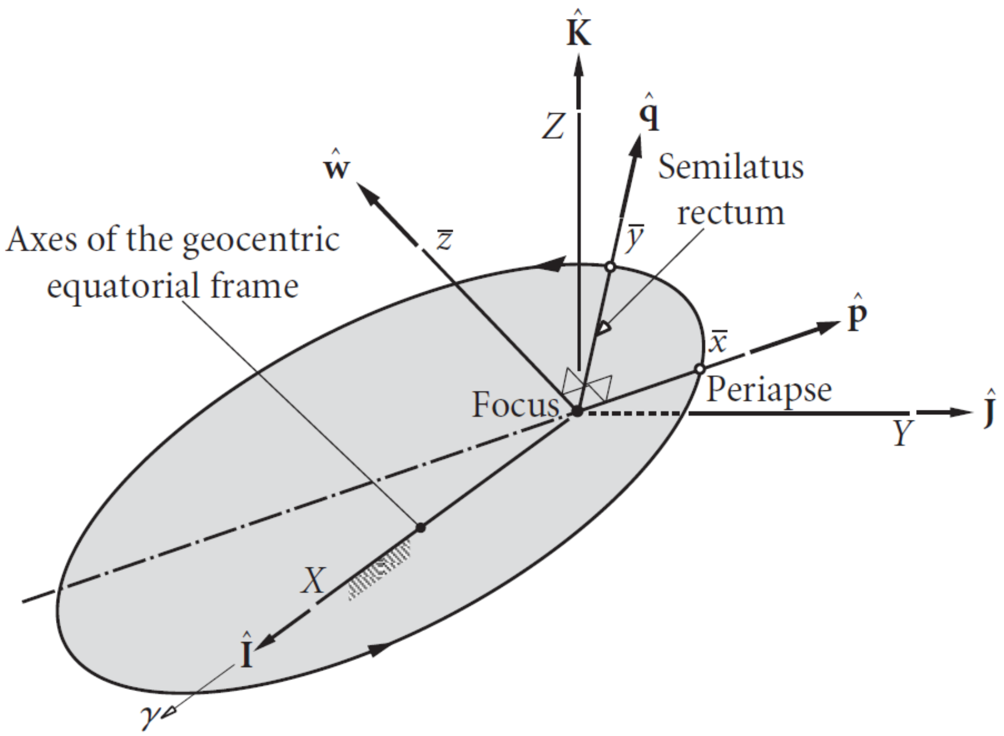

Figure 3.1: Perifocal $\hat{x}\hat{y}\hat{z}$ and geocentric-equatorial (XYZ) coordinate system. Figure extracted from [9].

Coordinate transformations

If the vector components are known in a certain coordinate system, it is possible to determine the vector in an other reference frame by using a coordinate transformation.

Every transformation between two Cartesian coordinate system can be expressed as a sequence of two-dimensional rotations defined by the following three matrices [9]

$$\mathbf{L}_1(\phi) = \begin{bmatrix} 1 & 0 & 0 \\ 0 & \cos\phi & \sin\phi \\ 0 & -\sin\phi & \cos\phi \end{bmatrix} \tag{3.1}$$

$$\mathbf{L}_2(\theta) = \begin{bmatrix} \cos\theta & 0 & -\sin\theta \\ 0 & 1 & 0 \\ \sin\theta & 0 & \cos\theta \end{bmatrix} \tag{3.2}$$

$$\mathbf{L}_3(\psi) = \begin{bmatrix} \cos\psi & \sin\psi & 0 \\ -\sin\psi & \cos\psi & 0 \\ 0 & 0 & 1 \end{bmatrix} \tag{3.3}$$

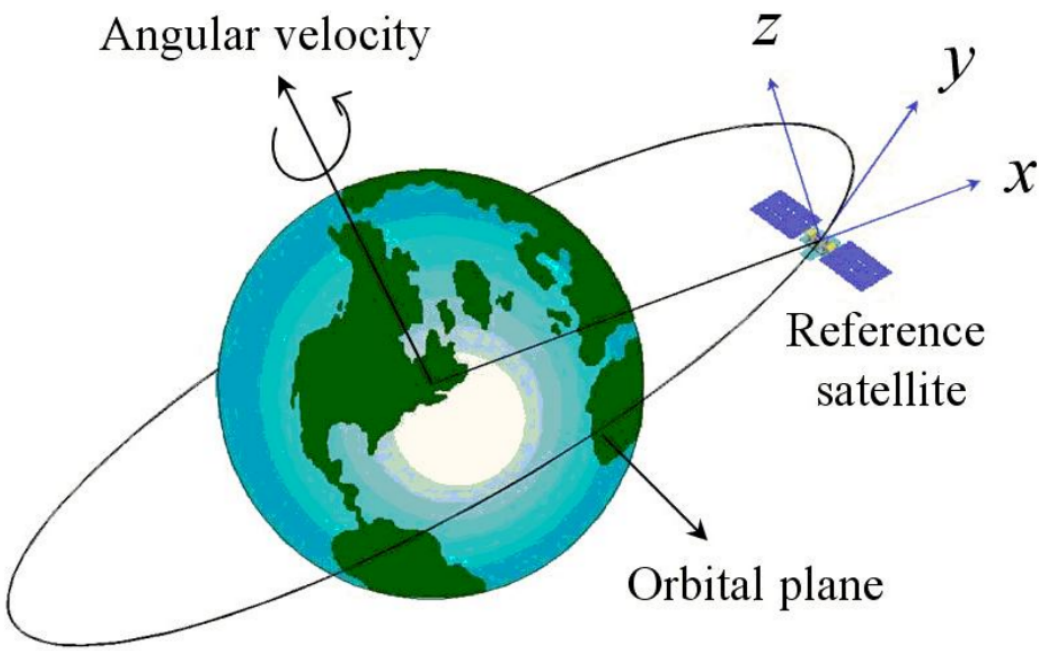

Figure 3.2: Local-Vertical Local-Horizontal coordinate system. Figure extracted from [15].

being ϕ, θ, ψ three generic rotation angles about the x, y and z axes, respectively. [9, 1]

The rotational matrix of the coordinate transformation from the perifocal to the geocentric-equatorial reference frame is

$$\mathbf{L}_{P\,I} = \mathbf{L}_3(\omega)\mathbf{L}_1(i)\mathbf{L}_3(\Omega) \tag{3.4}$$

where ω is the argument of periapsis, i is the orbit inclination and Ω is the right-ascension of the ascending node. [9, 1]

The transformation from the LVLH to the geocentric-equatorial coordinate system is defined by

$$\mathbf{L}_{L\,I} = \mathbf{L}_3(\omega + \nu)\mathbf{L}_1(i)\mathbf{L}_3(\Omega) \tag{3.5}$$

where ν is the true anomaly.

3.2.2 Determination of position and velocity in function of time

The trajectory equation (Eq. 3.6, which is equivalent to the equation of a conic section) relates the true anomaly with the modulus of the position. It is obtained by the integration of the equation of motion for the two-body problem as shown in [1].

$$r = \frac{p}{1 + e \cdot cos(\nu)} \tag{3.6}$$

where:

- r is the modulus of the position vector;
- $p = a(1 - e^2)$ is the semilatus rectum;
- e is the eccentricity;
- ν is the true anomaly.

With some geometrical consideration on the geometry of the ellipse and on the elliptical orbit period, it is possible to relate the time t_k with the eccentric anomaly E_k, as shown in [1]

$$t_k = \sqrt{\frac{a^3}{\mu}}(E_k - e \cdot \sin(E_k)) \tag{3.7}$$

where $M = E_k - e \cdot \sin(E_k) = t_k \cdot \sqrt{\mu/a^3}$ is called mean anomaly. The true anomaly, ν_k, can be related to E_k, at time t_k:

$$\nu_k = 2 \cdot \text{atan}\Big(\tan(E_k/2)\sqrt{(1+e)/(1-e)}\Big); \tag{3.8}$$

The time t_k is the time at which the spacecraft position and velocity have to be known. E_k can be retrieved, known t_k, solving Eq. 3.7 with numerical methods. The true anomaly at time t_k, ν_k, is found substituting E_k in Eq. 3.8. Thus, the modulus of position vector, r, can be simply obtained substituting the true anomaly ν_k in the trajectory equation (Eq. 3.6).

Now, the position and velocity vectors expressed in the perifocal coordinate system can be determined as follows:

$$\begin{aligned}
\mathbf{r}_{SC_{PQW}} &= \begin{Bmatrix} r \cdot \cos\nu \\ r \cdot \sin\nu \\ 0 \end{Bmatrix} \\
\mathbf{v}_{SC_{PQW}} &= \frac{\mu}{h} \cdot \begin{Bmatrix} -\sin\nu \\ e + \cos\nu \\ 0 \end{Bmatrix}
\end{aligned} \tag{3.9}$$

where μ is the Earth's gravitational parameter and $h = \sqrt{\mu \cdot p}$ is the modulus of the orbit's angular momentum.

Thus, from the starting orbital parameters, shown in tables 3.1 and 3.2, and defining a time discretization, it is possible to propagate the orbit and determine the position of the spacecraft, $\mathbf{r}_{SC_{PQW}}(t)$, and the velocity, $\mathbf{v}_{SC_{PQW}}(t)$, for every time instant, both expressed in the perifocal reference frame.

Those vectors can be also expressed in the geocentric-equatorial coordinate system by applying the corresponding coordinate transformation:

$$\begin{aligned} \mathbf{r}_{SC_{IJK}} &= \mathbf{L}_{PI}^{T} \cdot \mathbf{r}_{SC_{PQW}} \\ \mathbf{v}_{SC_{IJK}} &= \mathbf{L}_{PI}^{T} \cdot \mathbf{v}_{SC_{PQW}} \end{aligned} \tag{3.10}$$

where $\mathbf{L}_{PI} = \mathbf{L}_3(\omega(t))\mathbf{L}_1(i)\mathbf{L}_3(\Omega(t))$ is the transformation matrix between the two coordinate systems. Note that the argument of perigee, ω and the Right Ascension of the Ascending Node (RAAN), Ω, are time dependant. For simplicity, $\mathbf{r}_{SC_{IJK}}$ will be denoted by $\mathbf{r}_{SC}$.

3.2.3 J2 Perturbations and sun-synchronous orbits

The oblateness shape of the Earth causes orbit perturbation on the RAAN, the argument of periapsis and the mean anomaly. These three orbital elements are a function of time and their changing rate is defined as follow [8]:

$$\dot{\Omega} = -\frac{3}{2(1-e^2)^2} n J_2 \left(\frac{R_E}{a}\right)^2 \cos(i) \tag{3.11}$$

$$\dot{\omega} = \frac{3}{4(1-e^2)^2} n J_2 \left(\frac{R_E}{a}\right)^2 \left(5\cos^2(i) - 1\right) \tag{3.12}$$

$$\dot{M} - n = \Delta n = \frac{3}{4(1-e^2)^{3/2}} n J_2 \left(\frac{R_E}{a}\right)^2 \left(3\cos^2(i) - 1\right) \tag{3.13}$$

where R_E is the Earth radius, $n = \sqrt{\frac{\mu_E}{a}}$ is the Keplerian mean motion, μ_E is the Earth gravitational parameter and a is the orbit semi-major axis and i is the orbital inclination. $J2$ represent the second zonal harmonic and quantifies the oblateness of the planet, $J2 = 1.08263 \cdot 10^3$ for planet Earth.

Therefor, if the J2 perturbations are taken into account, the orbital elements at any time instant t can be easily determined at any time instant t as

$$\begin{aligned} a(t) &= a_0 & e(t) &= e_0 & i(t) &= i_0 \\ \Omega(t) &= \Omega_0 + \dot{\Omega}t & \omega(t) &= \omega_0 + \dot{\omega}t & M(t) &= M_0 + \dot{M}t \end{aligned} \tag{3.14}$$

the semi-major axis, the eccentricity and the inclination remains constant. While the other three change with time.

The variation of the RAAN can be translated as a rotation of the orbital plane in the inertial space. A desired variation of RAAN (see Eq. 3.11) can be obtained by choosing a certain combination of the orbital elements a, i and e. In sun-synchronous orbits, those orbital elements are chosen such as the RAAN variation rate keeps the angle between the orbital plane and the radial to the Sun constant, This is achieved by having a precession rate of the orbital plane equal to one revolution per sidereal year, which means $\dot{\Omega} = 1.99096871\text{E-7}\,\text{rad/s}$. Consequently, With the orbital plane rotating eastward at this rate, the ascending node will remain fixed at a certain Local Time.

When the satellites orbits are propagated, the new orbital parameters have to be calculated for every time interval of the integration.

3.2.4 From geocentric-equatorial to Earth-centered Earth-fixed (ECEF) reference frame

Expressing a vector in the ECEF reference frame is necessary in order compute the distance between two position fixed on the Earth surface, such as metereological targets illuminated by the radars.

The position vector at any time t can be expressed in an ECEF reference frame with the following coordinate transformation:

$$\mathbf{r}_{ECEF} = \mathbf{L}_3(\alpha_G(t))\mathbf{r}_{IJK} \tag{3.15}$$

where $\alpha_G(t)$ is the right ascension of the Greenwich meridian at time t. It is measured from the vernal equinox direction, which is equivalent to the unit vector $\hat{\mathbf{I}}$ of the geocentric-equatorial reference frame. The angle $\alpha_G(t)$ can be computed by:

$$\alpha_G(t) = \alpha_{G\,ref} + \omega_{E_D}\,(t_D - t_{D\,ref}) + \omega_E t \tag{3.16}$$

where $\alpha_{G\,ref}$ is the right ascension of the Greenwich meridian at time $t_{D\,ref}$, corresponding to the reference date 1 January 2000, 12:00 UT[1]. The term t_D represents the time at which the propagation starts (epoch of the orbit). Both $t_{D\,ref}$ and t_D are expressed in Julian Days. The time t is the time (in seconds) elapsed after the date t_D. Therefore, the Earth's angular velocity $\omega_E\,D$ is expressed in [rad/day] and ω_E in [rad/s].

Precession and nutation of the Earth's rotational axis cause the two reference frames to have their z-axis not aligned. Although, for simplicity, they are considered to be negligible, causing the alignment of the z-axis.

[1]This reference date is named J2000 epoch.

3.2.5 Latitude and longitude

Known at any time t the position vector $\mathbf{r} = \{x, y, z\}$ expressed in the geocentric equatorial reference frame, the latitude can be found as:

$$La = arcsin\left(\frac{z}{\|\mathbf{r}\|}\right) \tag{3.17}$$

and the longitude as:

$$Lo = \alpha - \alpha_G \tag{3.18}$$

where α is the right ascension of the position vector and α_G is the right ascension of the Greenwich meridian. Both angles are measured with respect to the vernal equinox direction ($\hat{\mathbf{I}}$ unit vector of the geocentric equatorial reference frame). The angle α can be calculated as follow with trigonometric observations:

$$\begin{cases} \alpha = \text{atan}_2(y, x) & \text{if } y \geq 0 \\ \alpha = 2\pi + \text{atan}_2(y, x) & \text{if } y < 0 \end{cases} \tag{3.19}$$

The angle α_G can be retrieved as shown in Eq. 3.16.

3.3 Antenna boresight vector

In this section, the procedure to determine the position vector of the footprint of a radar (denoted as $\mathbf{r}_S$) is described. Once the satellite positions have been computed for the whole simulation time, the antenna pointing direction is calculated at any time instant of the propagation, in order to determine the antenna boresight vector ($\mathbf{s}$), which define the relative position of a point illuminated by the radar with respect to the radar. Then, the position of such points are determined with respect to the center of the geocentric-equatorial reference frame. In other words, the position vector of the radars footprints with respect to the center of the Earth are computed.

For the along-track scanning radars pointing at nadir, the antenna boresight direction points from the radar towards the center of the Earth. Therefore the direction of the position vector of a target illuminated by the radar coincides with the satellite position vector, while its modulus is equal to the Earth radius. Note that, for a spaceborne radar operating with this type of scanning, the satellite and the radar ground-track are coincident.

For other type of scanning (i.e conical and cross-track) being in a Local-Vertical Local-Horizontal (LVLH) coordinate system is more convenient in order to find the antenna boresight vector. The spacecraft attitude is considered to be perfect, hence the LVLH frame is assumed to be identical to the body frame.

Conical scanning

Both Tomorrow.io and Wivern antennas scan around Nadir. For this type of scanning, the boresight direction is defined by the Off-Nadir pointing angle γ and the offset angle $\delta(t)$. The angle γ is constant, the angle $\delta(t)$ changes with time as following:

$$\delta(t) = \delta_0 + \omega(t - t_0) \tag{3.20}$$

where δ_0 is the offset angle at time t_0 and ω is the antenna rotating velocity.

The boresight unit vector in the LVLH frame can be computed at any time with trigonometric relations:

$$\hat{\mathbf{u}}_{bs_{LVLH}} = \left\{ \begin{array}{c} -\cos\gamma \\ \sin\gamma\cos\delta(t) \\ \sin\gamma\sin\delta(t) \end{array} \right\} \tag{3.21}$$

Once the boresight direction has been found, its modulus can be computed. The geometry of this scanning is illustrated in Fig. 3.3 and it can be seen that through the *law of sines* applied to the triangle made by $\mathbf{r}_{SC}$, $\mathbf{s}$ and $\mathbf{r}_s$, it's possible to find the unknown vector modulus and angles. In particular:

- $\mathbf{r}_{SC}$ is known in modulus and direction;
- the direction of $\mathbf{s}$ is known from Eq. 3.21, the modulus is unknown;
- the modulus of $\mathbf{r}_s$ is known and equal to R_E, the direction is unknown;
- γ is the only known angle.

Angle β can be calculated using the law of sines:

$$\frac{\sin\beta}{r_{SC}} = \frac{\sin\gamma}{R_E}$$

which becomes:

$$\beta = \pi - \arcsin\left(r_{SC}\frac{\sin\gamma}{R_E}\right) \tag{3.22}$$

where r_{SC} is the modulus of $\mathbf{r}_{SC}$. Then, the angle θ can be simply obtained by:

$$\theta = \pi - (\beta + \gamma) \tag{3.23}$$

Finally, by applying again the law of sines, the modulus of $\mathbf{s}$ can be retrieved:

$$s = \frac{R_E}{\sin\gamma}\sin\theta \tag{3.24}$$

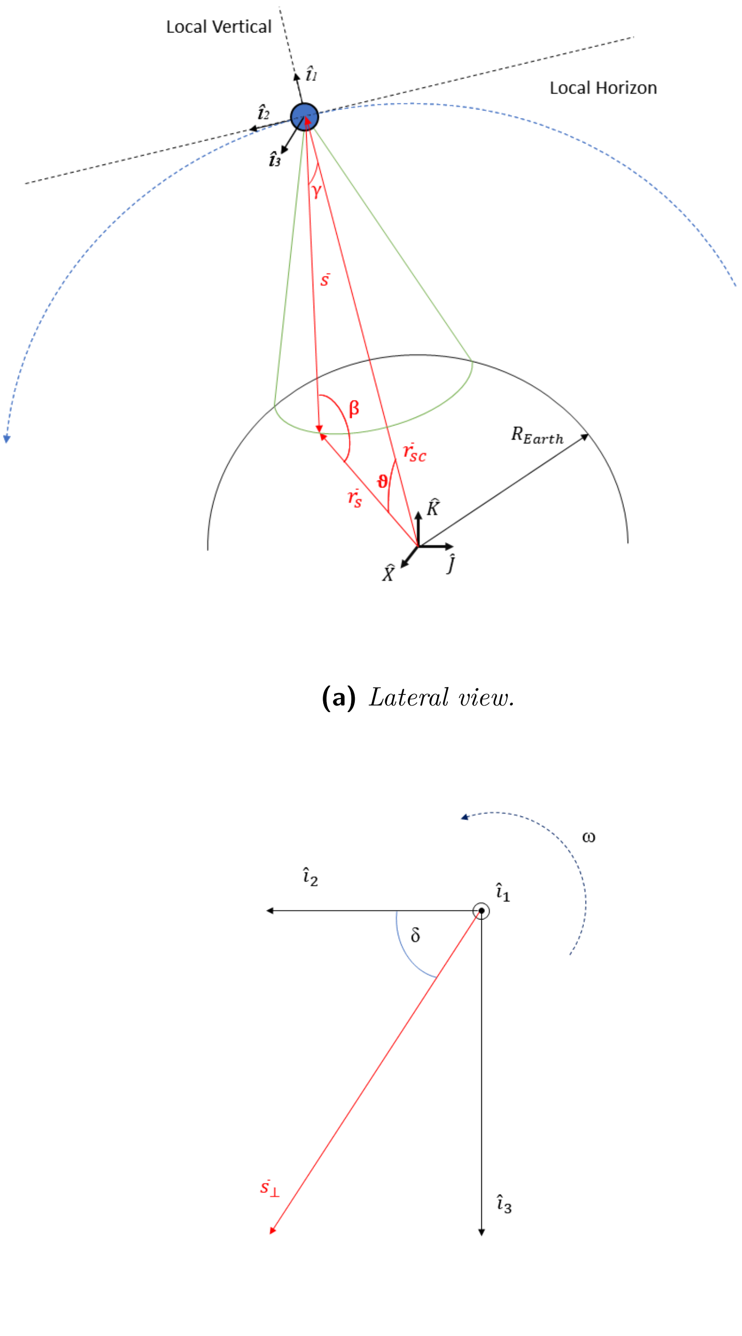

(a) *Lateral view.*

(b) *Frontal view.*

Figure 3.3: Geometry of a conically scanning radar.

The boresight vector ,**s**, is found in the LVLH reference frame with Eq. 3.21 and 3.24. It can be expressed in the geocentric equatorial frame thanks the following coordinate transformation:

$$\mathbf{s}_{IJK} = -\mathbf{L}_{L\,I}^{T}\mathbf{s}_{LVLH} \tag{3.25}$$

where $\mathbf{L}_{L\,I} = \mathbf{L}_3(\omega(t) + \nu(t))\mathbf{L}_1(i)\mathbf{L}_3(\Omega(t))$ is the rotational matrix between the two reference frames and $\nu(t)$ is the true anomaly.

At this point, known the boresight vector $\mathbf{s}_{IJK}$ and the position vector of the spacecraft $\mathbf{r}_{SC}$, the position of the point observed by the radar in the geocentric-equatorial frame, $\mathbf{r}_{s_{IJK}}$, can be simply computed as follow:

$$\mathbf{r}_{S_{IJK}} = \mathbf{s}_{IJK} + \mathbf{r}_{SC} \tag{3.26}$$

Cross-track scanning

GPM performs a cross-track scanning passing through the nadir. The off-nadir pointing angle γ is time dependant and varies in the range of values from $-\gamma_{max}$ to γ_{max}. The boresight vector lays on the LVLH $\hat{\mathbf{i}}_1 - \hat{\mathbf{i}}_3$ plane, which means its $\hat{\mathbf{i}}_2$ component is equal to zero. Therefore, the boresight direction is defined only by the off-Nadir pointing angle γ. The geometry of this type of scanning is depicted in Fig. 3.4.

GPM radar makes a complete swath scan every time the satellite covers a distance equal to the horizontal along-track resolution of the instrument. I.e., for GPM, the instrument makes a 245 km swath width scan every 5 km covered by the spacecraft. The angle γ has been computed for every time instant t as follow

$$\gamma_k = \gamma_{k-1} + \omega \cdot dt$$

where γ_k is the off-Nadir pointing angle at time $t = t_k$, γ_{k-1} is the angle at the previous time instant t_{k-1}, dt is the time discretization interval and ω is the scanning velocity. Every time the antenna reach the off-Nadir pointing angle equal to $-\gamma_{max}$ or γ_{max}, the velocity ω changes sign.

The boresight unit vector can be computed at any time with the following relations

$$\hat{\mathbf{u}}_{bs_{LVLH}} = \left\{ \begin{array}{c} 0 \\ -\cos\gamma(t) \\ \sin\gamma(t) \end{array} \right\} \tag{3.27}$$

Once the boresight unit vector in known, the boresight vector, both in the LVLH and geocentric-equatorial frame, can be determined with a very similar procedure to that illustrated for the conical scanning. Angle β can be retrieved using the law of sines:

$$\frac{\sin\beta}{r_{SC}} = \frac{\sin\gamma}{r_s}$$

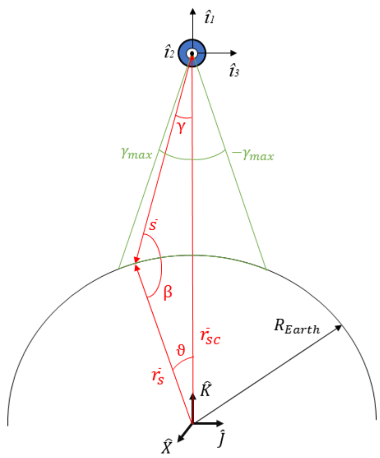

(a) *Frontal view.*

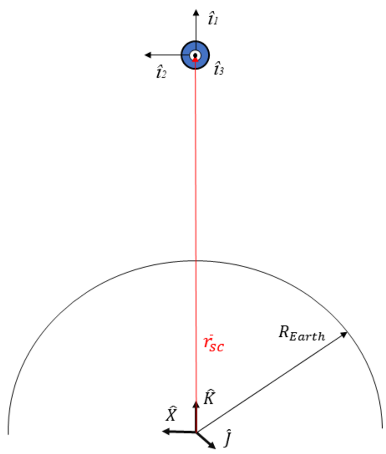

(b) *Lateral view.*

Figure 3.4: Geometry of a cross-track scanning radar.

The modulus of r_S is known and it is equal to the Earth's radius R_E. Thus, the previous equation becomes

$$\beta = \pi - \arcsin\left(r_{SC}\frac{\sin|\gamma|}{R_E}\right) \tag{3.28}$$

Angle θ is found as

$$\theta = \pi - (\beta + |\gamma|) \tag{3.29}$$

By applying again the law of sines, the modulus of $\mathbf{s}$ is obtained:

$$s = \frac{R_E}{\sin|\gamma|}\sin\theta \tag{3.30}$$

The boresight vector is now defined thanks to Eq. 3.27 and Eq. 3.30 in the LVLH reference frame. It can be expressed in the geocentric-equatorial coordinate system by applying the transformation

$$\mathbf{s}_{IJK} = -\mathbf{L}_{L\,I}^{T}\mathbf{s}_{LVLH} \tag{3.31}$$

where $\mathbf{L}_{L\,I} = \mathbf{L}_3(\omega(t) + \nu(t))\mathbf{L}_1(i)\mathbf{L}_3(\Omega(t))$ is the rotational matrix between the two reference frames.

At the end, the position of the point observed by the radar in the geocentric-equatorial system, $\mathbf{r}_{S_{IJK}}$, can be easily obtained as follow

$$\mathbf{r}_{S_{IJK}} = \mathbf{s}_{IJK} + \mathbf{r}_{SC_{IJK}} \tag{3.32}$$

Note that the procedure for the determination of the boresight position in the geocentric-equatorial reference frame for a cross-scanning radar is very similar to that used for the conically scanning radar. The differences are in the computation of the boresight unit vector and in the angle γ, which is constant for a conically scanning radar and is a function of time for the cross scanning radar.

3.4 Computation of intersection points

First, for each sun-synchronous orbit, the RAAN at time t_0 is derived from the Mean Local Time of the Ascending Node (MTLAN).
To do so, the hour of the spacecraft Epoch t_0 has been set equal to the orbit's MLTAN. The spacecraft is imposed to be, at time t_0 of its Epoch, at the ascending node and on the Greenwich meridian, hence at longitude= 0°. This also means the right ascension of the position vector is equal to the right ascension of the ascending node ($RAAN = \alpha$).
The angle α_G can be calculated with Eq 3.16. Known the longitude ($Lo = 0$) and α_G, the angle α, and the RAAN, can be easily retrieved with Eq. 3.19.

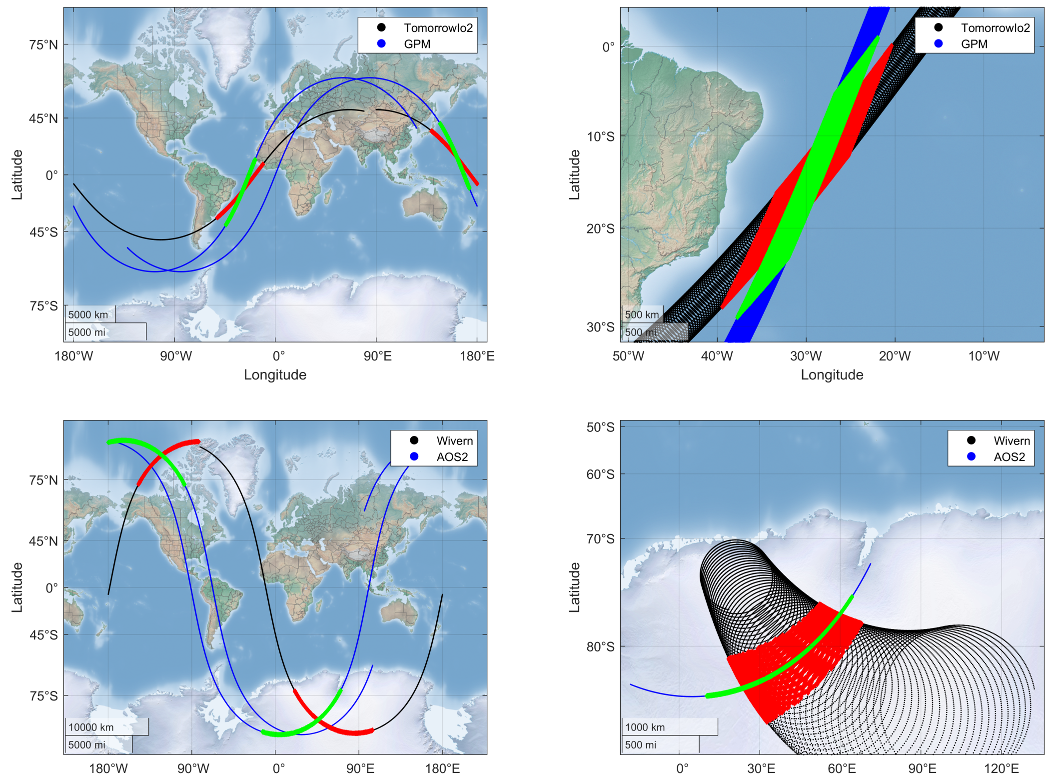

Figure 3.5: Intersection between Tomorrow.io2 and the Ka-DPR radar (top panels) and the AOS2 polar W-band radar and the conically scanning Wivern radar (bottom panels) according to criterion #11 ($\Delta t = 30$ minutes, $\Delta r = 200$ km). The left panels depicts the ground tracks of the two orbits and the right panels shows the details of the two radar footprints at the ground in the region where the ground-tracks intersect. Figures submitted in [4].

Selected an intersection criterion (reported in table 3.3), the coincidence points have been computed for a period of 365 days. This procedure has been divided into two phases.
The goal of *Phase 1* is to determine the time intervals in which the satellites are enough close to make happen an intersection. In *Phase 2*, the positions of the footprint of the radars have been computed for any coincidence criterion, with a higher time resolution than the one used in phase one. This procedure is illustrated in Fig. 3.5.

Phase 1 consists in the following procedure:

1. The simulation time is discretized into equally spaced time values. The position

vector, at ground, of both spacecraft A and B is computed for each value of t (as shown in 3.2.2).

2. Each position vector expressed in the geocentric-equatorial reference frame has been transformed in order to be expressed in an Earth-centered Earth-fixed coordinate system.

3. For every time t, the spherical distances, over a sphere of radius equal to the R_E, between the position of spacecraft A at time t and the position of spacecraft B from time $t - \Delta t$ to time $t + \Delta t$ have been computed.

4. the values of time where the distance computed above is lower than $\dfrac{swath\_width_A + swath\_width_B}{2} + \Delta r$ are saved and used in the *Phase 2*.

At the end of this phase, we have obtained the time intervals when the ground distance between the two satellites is lower enough to permit the intersection happen according to the selected criterion.

For every time interval calculated in *Phase 1*, the procedure used in *Phase 2* to compute the number of intersection points is the following:

1. Each time interval found in *Phase 1* is discretized in equally spaced time values.

2. For every time t of the interval, the position vectors of satellite A and B are determined in the perifocal reference frame and then expressed in the geocentric-equatorial coordinate system by applying the corresponding coordinate transformation, as shown in section 3.2.2.

3. From the position vectors of the satellites computed above, the position of points observed by the instrument A and B (their footprints) expressed in the geocentric-equatorial frame are calculated as described in section 3.3.

4. The vectors obtained above have been expressed in the ECEF reference frame through another coordinate transformation in order to take account of the Earth's rotation (as shown in 3.2.4). This phase is necessary because we are interested in the relative position of targets illuminated by the radars, which, thus, are fixed on the Earth surface. Now we have the position of the footprints of instrument A, expressed in the ECEF reference frame, for every time t of the time interval considered. We have the same for the instrument B.

5. For every point A_i of footprint A, if there is at least one point of footprint B that satisfies the distance and time conditions of the selected intersection criterion with point A_i, A_i is coincidence point. The same has been done for B respect to A. The distance taken in account here is a spherical distance on a sphere of radius equal to R_E.

6. The latitude - longitude coordinate of every intersection point computed above has been found as shown in section 3.2.5.

This procedure is repeated for every intersection criteria.

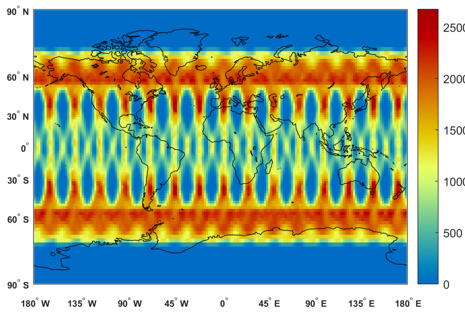

(a) *Tomorrow.io1 - GPM*

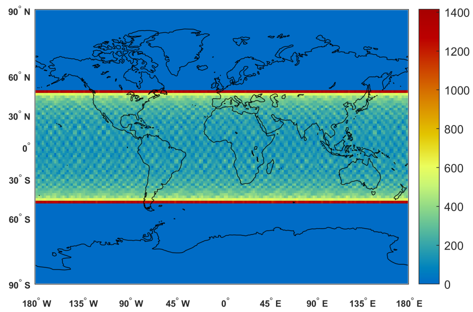

(b) *Wivern - AOS1*

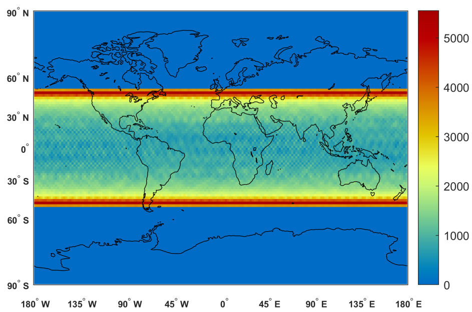

(c) *Tomorrow.io2 - GPM*

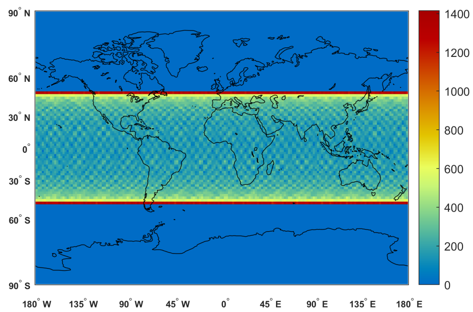

(d) *Wivern - AOS2*

Figure 3.6: Number of monthly intersection points and its global distribution of each of the four combinations of satellites according to criterion #13 ($\Delta t = 30$ minutes, $\Delta r = 1000\,\text{km}$). Figures submitted in [4].

At the end of this phase, for each intersection criterion, we have a Latitude - Longitude coordinate grid for each day that compose the simulation time, in which is reported for every coordinate the number of intersection points that occur at that coordinate.

The monthly mean of the number of calibration points per each coordinate is shown in Fig. 3.6 for criterion #13. It can be noticed that, in the case where both satellites have a polar sun-synchronous orbit (such as the Wivern - AOS2

combination), the angle between the two orbital planes remains constant and the ground-tracks and orbits intersections are located only near the poles. In the other cases those are distributed over all the globe. Also, as can be seen in Fig. 3.6, the lowest orbit inclination of the two satellites set a limit to the value of the maximum and minimum latitude covered by the intersections. The swath width of both radars and the Δr of the chosen criterion affects that limit. Higher swath width and higher Δr increase the range of latitudes covered.
The intersection points are clustered around the maximum and the minimum latitude covered.

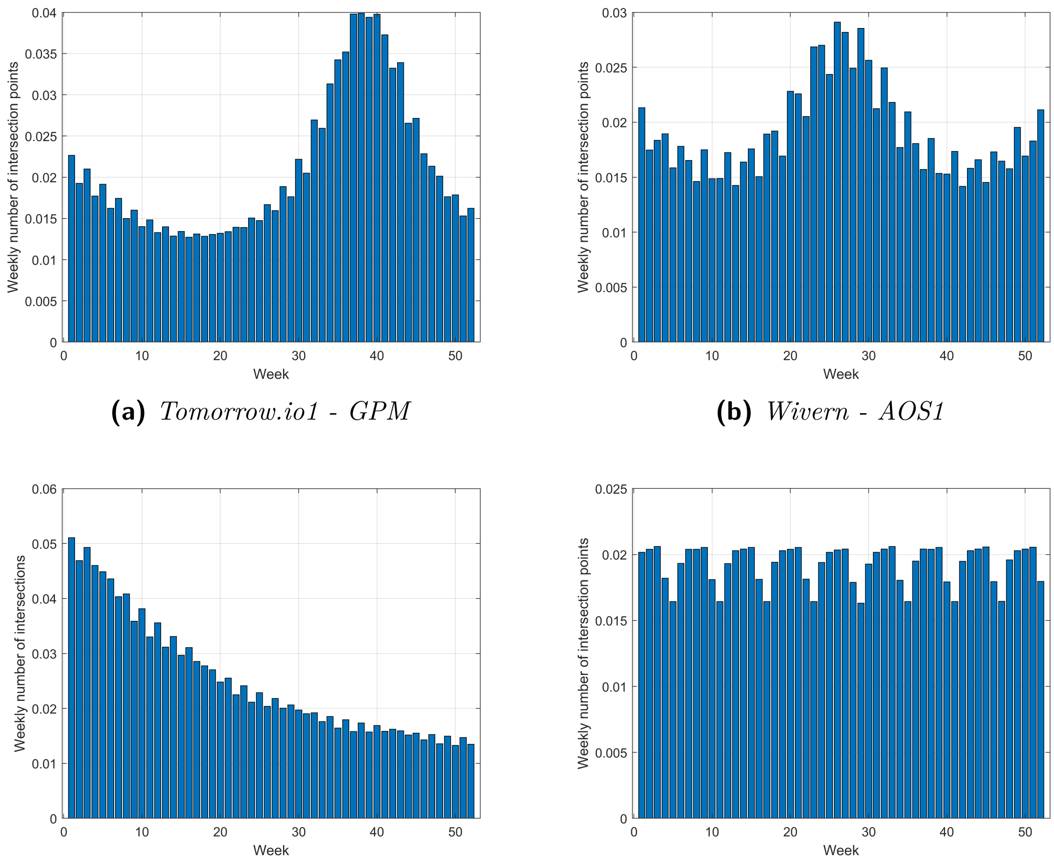

(a) *Tomorrow.io1 - GPM* **(b)** *Wivern - AOS1*

(c) *Tomorrow.io2 - GPM* **(d)** *Wivern - AOS2*

Figure 3.7: Weekly fraction of the intersection points for each of the four combinations of satellites according to criterion #13 ($\Delta t = 30$ minutes, $\Delta r = 1000\,\text{km}$). Figures submitted in [4].

As shown in Fig. 3.7, there is no much weekly variability of the intersection points for the Wivern - AOS combinations. Higher weekly variability is present for the combinations between Tomorrow.io and GPM. For the polar one, the cycle exceeds one year.

The mean number of intersection points per week for each satellite combination and for each intersection criterion is shown in Tab. 3.4. For each radar-pair configuration, the number of intersections has been computed over the footprint of both radars. The number of intersection points involving the Wivern radar are reported in columns from the 6^{th} to the 9^{th}. Due to its much higher scanning ground velocity ($\approx 800\,\mathrm{km\,s^{-1}}$) and its faster sampling rate, Wivern collects a considerably larger amount of intersection points than AOS radars. Whereas, the number of intersections collected by the Tomorrow.io and GPM radars are comparable due to their similar sampling rate.
As expected, the number of intersection points increases with Δt and Δr for all the radar configurations.

Table 3.4: Number of weekly intersection points. For each configuration the number of intersection points for each of the radars involved in the cross-calibration are reported in the two corresponding columns. An intersection point correspond to a 5 and 1 km along-footprint track for the Tomorrow.io and Wivern combinations, respectively.

Criterion	Tomorrow.io1-GPM		Tomorrow.io2-GPM		Wivern-AOS1		Wivern-AOS2	
	# intersection points per week							
1	1.59×10^5	3.71×10^5	3.33×10^5	7.39×10^5	3.10×10^5	8.63×10^4	2.63×10^5	7.04×10^4
2	1.92×10^5	4.14×10^5	4.01×10^5	8.24×10^5	6.21×10^5	9.17×10^4	5.28×10^5	7.48×10^4
3	2.55×10^5	5.00×10^5	5.34×10^5	9.95×10^5	1.25×10^6	1.03×10^5	1.06×10^6	8.36×10^4
4	3.84×10^5	6.74×10^5	8.06×10^5	1.35×10^6	2.54×10^6	1.25×10^5	2.15×10^6	1.02×10^5
5	7.90×10^5	1.34×10^6	1.67×10^6	2.71×10^6	6.58×10^6	1.94×10^5	5.57×10^6	1.58×10^5
6	1.53×10^6	2.51×10^6	3.35×10^6	5.29×10^6	1.40×10^7	3.21×10^5	1.18×10^7	2.59×10^5
7	3.28×10^6	5.20×10^6	8.20×10^6	1.25×10^7	3.15×10^7	6.18×10^5	2.62×10^7	4.93×10^5
8	3.11×10^5	7.16×10^5	6.56×10^5	1.43×10^6	6.11×10^5	1.66×10^5	5.28×10^5	1.38×10^5
9	3.74×10^5	7.97×10^5	7.88×10^5	1.60×10^6	1.22×10^6	1.77×10^5	1.06×10^6	1.47×10^5
10	4.96×10^5	9.60×10^5	1.05×10^6	1.93×10^6	2.46×10^6	1.97×10^5	2.12×10^6	1.63×10^5
11	7.42×10^5	1.29×10^6	1.57×10^6	2.59×10^6	4.94×10^6	2.38×10^5	4.27×10^6	1.97×10^5
12	1.50×10^6	2.52×10^6	3.19×10^6	5.13×10^6	1.26×10^7	3.63×10^5	1.09×10^7	3.02×10^5
13	2.83×10^6	4.60×10^6	6.20×10^6	9.68×10^6	2.60×10^7	5.83×10^5	2.24×10^7	4.83×10^5
14	5.77×10^6	9.08×10^6	1.44×10^7	2.18×10^7	5.54×10^7	1.07×10^6	4.76×10^7	8.78×10^5
15	4.55×10^5	1.04×10^6	9.62×10^5	2.10×10^6	8.93×10^5	2.41×10^5	7.94×10^5	2.06×10^5
16	5.46×10^5	1.16×10^6	1.16×10^6	2.34×10^6	1.79×10^6	2.56×10^5	1.59×10^6	2.19×10^5
17	7.24×10^5	1.40×10^6	1.53×10^6	2.81×10^6	3.58×10^6	2.85×10^5	3.19×10^6	2.44×10^5
18	1.08×10^6	1.87×10^6	2.29×10^6	3.77×10^6	7.19×10^7	3.43×10^5	6.40×10^6	2.94×10^5
19	2.17×10^6	3.65×10^6	4.64×10^6	7.43×10^6	1.82×10^7	5.20×10^5	1.62×10^7	4.46×10^5
20	4.06×10^6	6.59×10^6	8.93×10^6	1.39×10^7	3.70×10^7	8.23×10^5	3.27×10^7	6.98×10^5
21	7.98×10^6	1.25×10^7	1.71×10^7	2.63×10^7	7.66×10^7	1.44×10^6	6.55×10^7	1.20×10^6

Chapter 4

Climatology of the ice calibrating clouds

Ice clouds away from deep convection are chosen as natural targets for the cross-calibration. Such clouds cause negligible signal attenuation both at Ka and W-band. Therefore their reflectivity do not change with different observation geometries (i.e. the measured reflectivity of an ice cloud observed at nadir and at slant incidence angles are almost the same). Different selection criterion are used for the two bands due to the different sensitivities of the two reference radar.

A cloud climatology study of Ka-band and W-band clouds has been done respectively with GPM KaPR and CloudSat CPR datasets. Those datasets can be exploited to understand where the calibration targets are located and how frequently they occur.

4.1 W-band clouds climatology

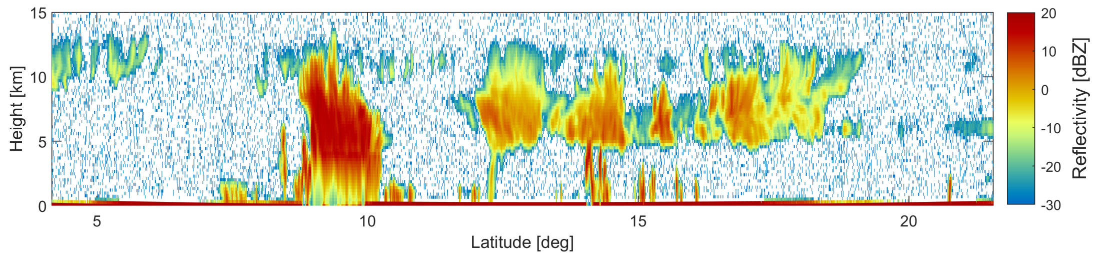

Figure 4.1: An example plot of 2B-GEOPROF reflectivities on December 31, 2007.

Ice clouds with the following properties have been chosen as natural calibration targets for the W-band radar systems:

- Temperature lower than 250 K to identify ice clouds;
- Reflectivity exceeding -20 dBZ (Wivern will certainly have such sensitivity [13]);
- Height: above 2 km from the clutter;
- Vertical extension of at least 750 m;
- Deep convective cores have been excluded.

CloudSat CPR dataset has been used to understand where such W-band clouds are located and how frequently they occur, due to its better sensitivity of around -30 dBZ.

Data products are formatted through two dimensions. The first dimension corresponds to the number of rays, *nrays*. Each ray corresponds to a vertical profile. The second dimension corresponds to the binning of the profiles, menaing that each vertical profile is divided in a certain number of bins, *nbins*, that, for CloudSat dataset, is equal to 125. It can be seen as a division of each vertical profile in *nbins* number of horizontal intervals.

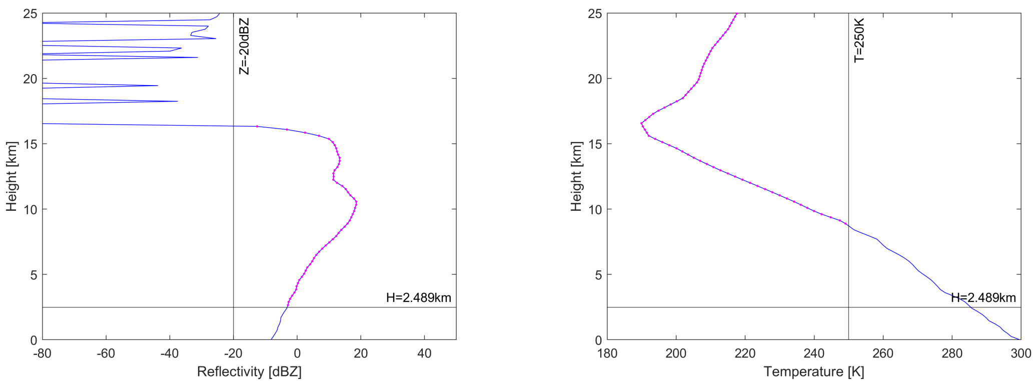

(a) *Reflectivity profile* **(b)** *Temperature profile*

Figure 4.2: Example of a reflectivity profile and a temperature profile for a single ray sampled by CloudSat. The magenta dots represents the points which satisfy the reflectivity and height (a), and temperature and height conditions (b).

Different data products [22] have been used in this analysis; they are the following:

- **2B GEOPROF**
    - Latitude: indicates the latitude of each profile;

  - Longitude: indicates the longitude of each ray;
  - Reflectivity: indicates the value of reflectivity in every bin of each profile;
  - Height: indicates the altitude of every bin of each profile;
  - SurfaceHeightBin: indicates the bin that correspond to the clutter in each profile;

- **ECMWF-AUX**

  - Temperature: indicates the value of temperature on every bin of each profile.

- **2B CLDCLSS**

  - CloudLayerType: indicates the type of cloud layer for every bin of each profile.

Those products have been used to determine the geo-located reflectivity profiles, to identify the surface clutter height, to obtain the temperature profiles and to exclude deep convective cores. An example of a W-band cloud system observed by CloudSat is shown in Fig. 4.1. An example of a reflectivity profile and a temperature profile is illustrated in Fig. 4.2. An example of a tropical cloud system is depicted in Fig. 4.6, in which the highlighted region identifies the points where the W-band calibration target conditions are satisfied, and thus the ice calibrating clouds.

Four years of data, from 2007 to 2010, have been used in order to compute the climatology of such clouds observed by the CloudSat radar. The global distribution of the mean number of 500 m-thick ice W-band calibrating clouds is shown in Fig. 4.3, while a separated plot for each different season is reported in Fig. 4.4. Thick ice clouds frequently occurs in region of deep convection, e.g. in the region called the Inter Tropical Convergence Zone, located near the equator and the tropics, and at mid latitudes. In some areas of the tropics, the mean number of 500 m thick ice layers is higher than one, therefore they are always present.

The zonal distribution of the ice calibrating layers is shown in Fig. 4.5 for the four seasons: DJF (December, January, February), MAM (March, April, May), JJA (June, July, August) and SON (September, October, November). In the tropical zone, the maximum is located at the south of the Equator in DJF and at the north of the Equator in JJA. The seasonal location of the maximum coincides with the location of the Intertropical Convergence Zone. Thicker ice clouds occur in the high latitude of the northern hemisphere during Summer (JJA) and Autumn (SON). While the mid and high latitude of the southern hemisphere have less variable ice cloud frequencies.

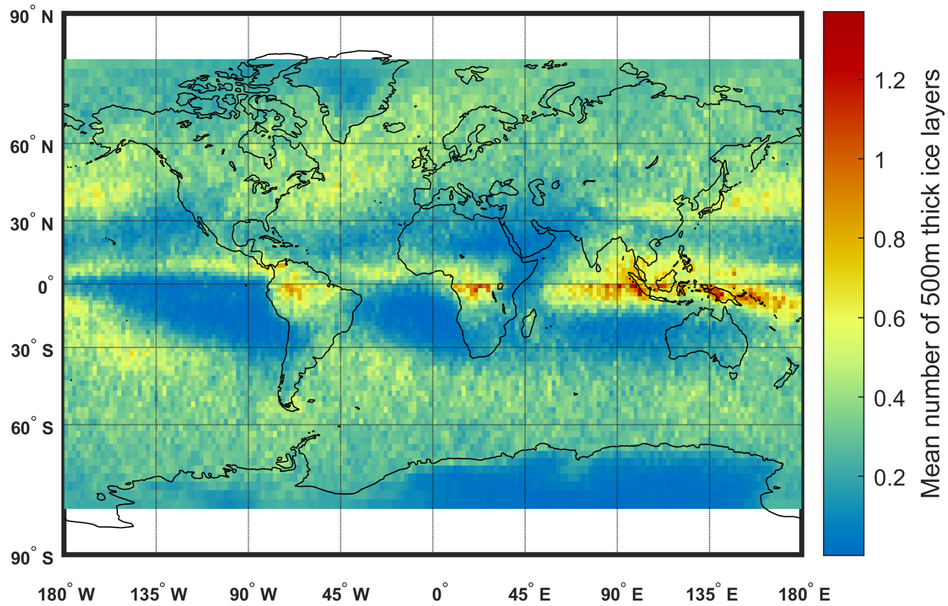

Figure 4.3: Global distribution of the mean number of 500 m thick ice layers of W-band calibrating clouds. The resolution is 2°× 2°. Figure submitted in [4].

4.2 Ka-band clouds climatology

The procedure described in the previous section has been repeated exploiting the GPM KaPR dataset in order to study the climatology of Ka-band clouds.

The ice clouds with reflectivity higher than 15 dBZ (a sensitivity that should be achieved by Tomorrow.io radar), located at least 500 m above the freezing level and the surface, and with a thickness of at least one kilometer are used as calibration targets for the Ka-band radars.

The KaPR GPM radar L2 products (zFactorMeasured, binZeroDeg, binClutterFreeBottom, https://gportal.jaxa.jp/gpr/assets/mng_upload/GPM/GPM_Product_List.pdf) have been used to determine where ice calibrating clouds are located and the frequency of their occurrence.

A GPM Ka-band reflectivity profiles plot of a mid-latitude cloud system is shown in the left panel of Fig. 4.6; the brighter regions of the picture represents the points belonging to ice calibrating clouds.

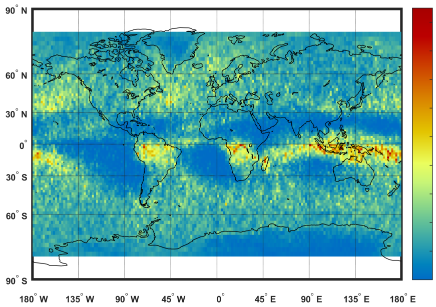

(a) *DJF*

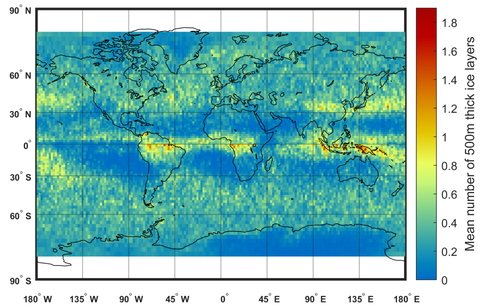

(b) *MAM*

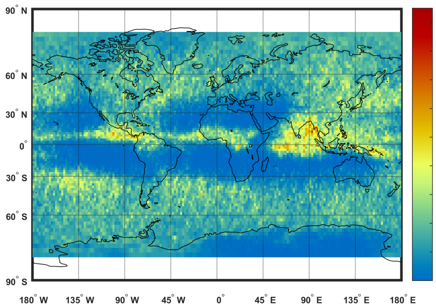

(c) *JJA*

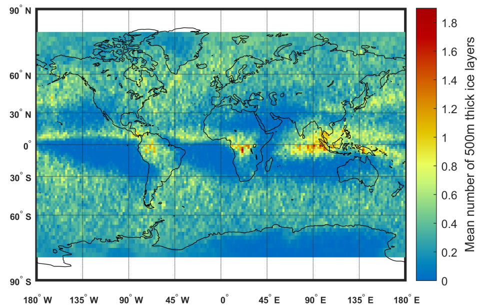

(d) *SON*

Figure 4.4: Distribution of the the mean number of 500 m thick ice layers of W-band calibrating clouds for four seasons: DJF - December, January, February; MAM - March, April, May; JJA - June, July, August; SON - September, October, November The resolution is 2°× 2°.

This statistical analysis is based on data collected in a four years time span, from the satellite launch happened in 2014 to May 2018, when the scanning strategy was modified.

The global distribution of the mean number of 500 m-thick ice Ka-band calibrating clouds is shown in Fig. 4.7. The patterns are very similar to those obtained for the W-band. The number of ice calibrating layers are also similar, the tighter constraint on temperature offsets the lower sensitivity at Ka-band. The seasonal zonal variability observed is similar to the one obtained at W-band as well. A comparable movement with the inter-tropical convergence zone is also detected.

These patterns obtained, bot at W and Ka-band, are coherent with the ones

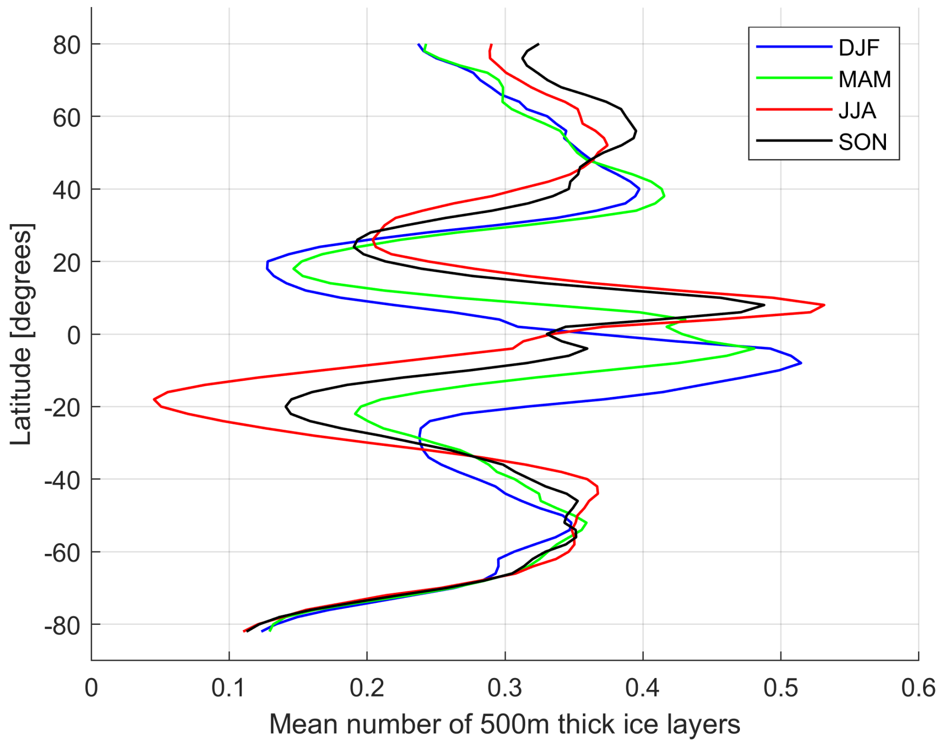

Figure 4.5: Zonal variability of the mean number of 500 m thick ice layers of W-band calibrating clouds. Four different season are plotted: DJF - December, January, February; MAM - March, April, May; JJA - June, July, August; SON - September, October, November. Figure submitted in [4].

obtained from CloudSat and Calipso in [12].

4.3 Calibration points

The result of the climatological study of the ice calibrating clouds is combined with the result of the intersections analysis in order to obtain the total number and the global distribution of the calibration points.

The global distribution of the calibration points is shown in Fig. 4.9. It is obtained by multiplying the global distribution of intersection points (see Fig. 3.6) by the global distribution of the mean number of ice calibrating layers (see Fig. 4.3 and 4.7). A calibration point correspond to a 5 and 1 km along-footprint track for the Ka and W-band, respectively.

The weekly distribution remains almost constant with no significant change of

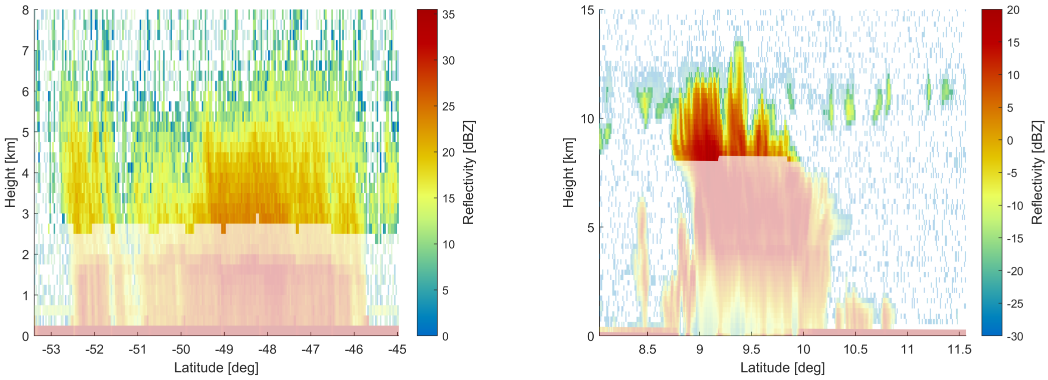

(a) *Ka-band* **(b)** *W-band*

Figure 4.6: Example of GPM Ka-band (a) and CloudSat W-band (b) reflectivity profiles respectively over a mid-latitude and a tropical cloud system. The brigther regions represents the points that are used as natural calibration target that satisfies the conditions listed above for the Ka-band and the W-band calibrating clouds. Figures submitted in [4].

number of calibration points or gaps along the weeks for the Wivern-AOS radar-pair, while a little variability is present for Tomorrow.io and GPM, as also observed for the intersections.

The number of calibration points of each satellite configuration is shown in Tab 4.1 for every combination of radar analyzed. As expected and already noticed in the previous chapter, the number of points increases with Δt and Δr.

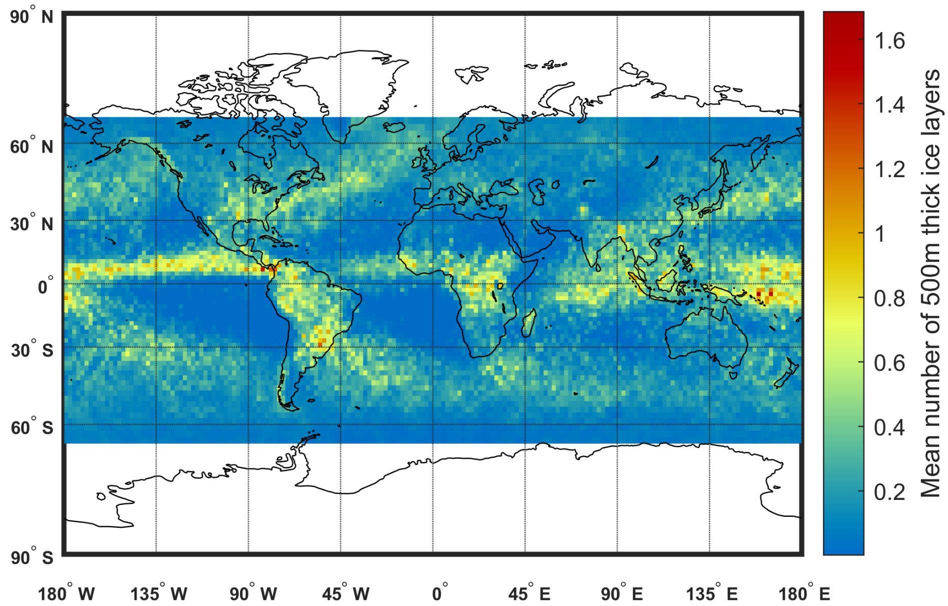

Figure 4.7: Global distribution of the mean number of 500 m thick ice layers of Ka-band calibrating clouds. The resolution is $2^\circ \times 2^\circ$. Figure submitted in [4].

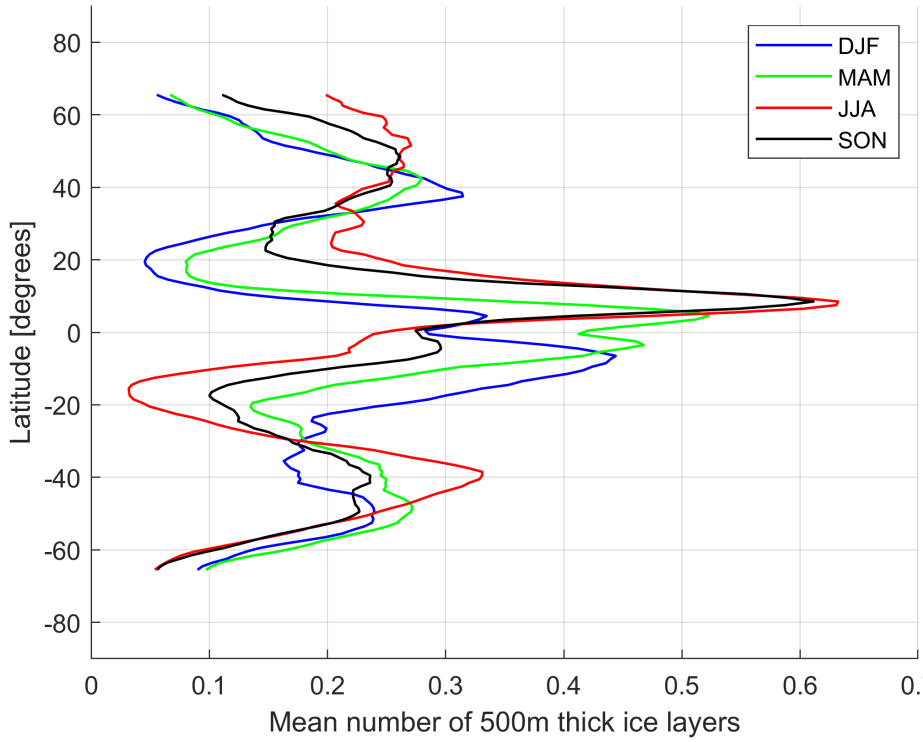

Figure 4.8: Zonal variability of the mean number of 500 m thick ice layers of Ka-band calibrating clouds. Four different season are plotted: DJF - December, January, February; MAM - March, April, May; JJA - June, July, August; SON - September, October, November. Figure submitted in [4].

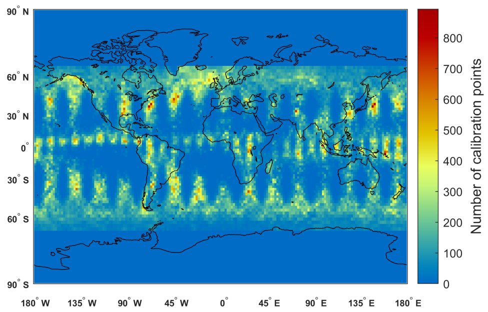

(a) *Tomorrow.io1 - GPM*

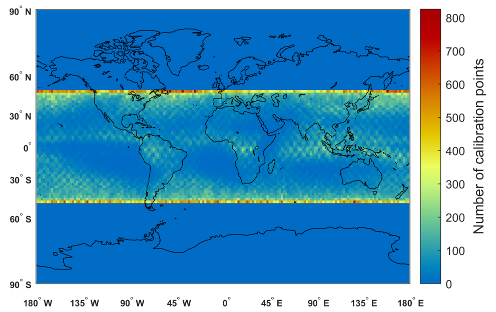

(b) *Wivern - AOS1*

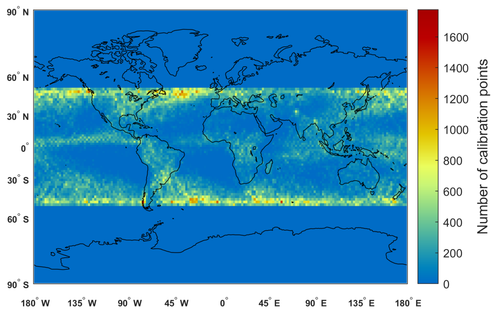

(c) *Tomorrow.io2 - GPM*

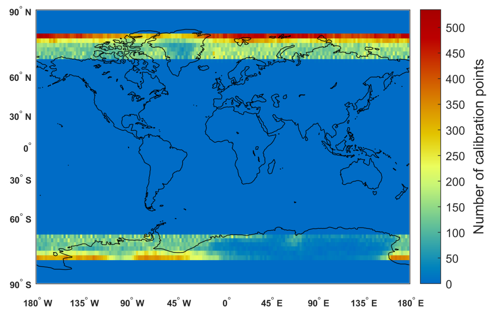

(d) *Wivern - AOS2*

Figure 4.9: Number of monthly calibration points and its global distribution for each of the four combinations of satellites according to criterion #13 ($\Delta t = 30$ minutes, $\Delta r = 1000\,\text{km}$).

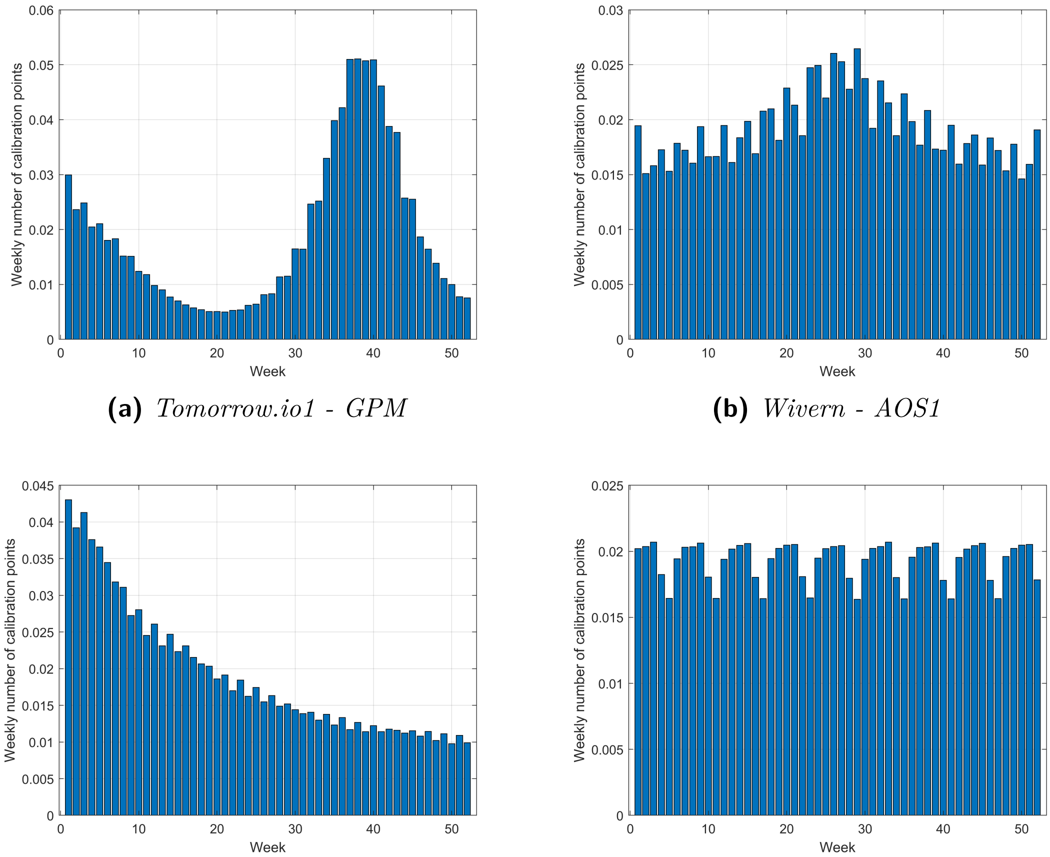

(a) *Tomorrow.io1 - GPM* **(b)** *Wivern - AOS1*

(c) *Tomorrow.io2 - GPM* **(d)** *Wivern - AOS2*

Figure 4.10: Weekly distribution of the calibration points for each of the four combinations of satellites for criterion #13 (Δt = 30 minutes, Δr = 1000 km).

Table 4.1: Mean number of weekly calibrating points. For each radar-pair configuration the number of calibrating points belonging to both radars involved are reported in two different columns. A calibration point corresponds to a 5 and 1 km along-footprint track for the Ka and W-band, respectively.

Criterion	Tomorrow.io1-GPM		Tomorrow.io2-GPM		Wivern-AOS1		Wivern-AOS2	
	# calibrating points per week							
1	$1.32{\times}10^{4}$	$2.16{\times}10^{4}$	$3.54{\times}10^{4}$	$5.52{\times}10^{4}$	$9.87{\times}10^{4}$	$2.76{\times}10^{4}$	$3.24{\times}10^{4}$	$9.56{\times}10^{3}$
2	$1.58{\times}10^{4}$	$2.41{\times}10^{4}$	$4.26{\times}10^{4}$	$6.18{\times}10^{4}$	$1.98{\times}10^{5}$	$2.93{\times}10^{4}$	$6.55{\times}10^{4}$	$1.00{\times}10^{4}$
3	$2.09{\times}10^{4}$	$2.91{\times}10^{4}$	$5.66{\times}10^{4}$	$7.52{\times}10^{4}$	$3.99{\times}10^{5}$	$3.29{\times}10^{4}$	$1.40{\times}10^{5}$	$1.09{\times}10^{4}$
4	$3.09{\times}10^{4}$	$3.91{\times}10^{4}$	$8.51{\times}10^{4}$	$1.03{\times}10^{5}$	$8.07{\times}10^{5}$	$4.00{\times}10^{4}$	$3.01{\times}10^{5}$	$1.28{\times}10^{4}$
5	$6.13{\times}10^{4}$	$7.70{\times}10^{4}$	$1.80{\times}10^{5}$	$2.09{\times}10^{5}$	$2.08{\times}10^{6}$	$6.15{\times}10^{4}$	$8.00{\times}10^{5}$	$1.97{\times}10^{4}$
6	$1.16{\times}10^{5}$	$1.43{\times}10^{5}$	$3.67{\times}10^{5}$	$3.90{\times}10^{5}$	$4.36{\times}10^{6}$	$1.00{\times}10^{5}$	$1.80{\times}10^{6}$	$4.14{\times}10^{4}$
7	$2.41{\times}10^{5}$	$2.98{\times}10^{5}$	$8.85{\times}10^{5}$	$8.09{\times}10^{5}$	$9.60{\times}10^{6}$	$1.92{\times}10^{5}$	$5.12{\times}10^{6}$	$9.94{\times}10^{4}$
8	$2.44{\times}10^{4}$	$3.96{\times}10^{4}$	$6.98{\times}10^{4}$	$1.08{\times}10^{5}$	$1.97{\times}10^{5}$	$5.37{\times}10^{4}$	$6.52{\times}10^{4}$	$1.86{\times}10^{4}$
9	$2.93{\times}10^{4}$	$4.41{\times}10^{4}$	$8.39{\times}10^{4}$	$1.21{\times}10^{5}$	$3.95{\times}10^{5}$	$5.69{\times}10^{4}$	$1.32{\times}10^{5}$	$1.95{\times}10^{4}$
10	$3.87{\times}10^{4}$	$5.33{\times}10^{4}$	$1.11{\times}10^{5}$	$1.46{\times}10^{5}$	$7.91{\times}10^{5}$	$6.34{\times}10^{4}$	$2.80{\times}10^{5}$	$2.12{\times}10^{4}$
11	$5.73{\times}10^{4}$	$7.18{\times}10^{4}$	$1.67{\times}10^{5}$	$1.98{\times}10^{5}$	$1.59{\times}10^{6}$	$7.63{\times}10^{4}$	$5.97{\times}10^{5}$	$2.48{\times}10^{4}$
12	$1.13{\times}10^{5}$	$1.40{\times}10^{5}$	$3.47{\times}10^{5}$	$3.97{\times}10^{5}$	$4.01{\times}10^{6}$	$1.15{\times}10^{5}$	$1.55{\times}10^{6}$	$3.79{\times}10^{4}$
13	$2.09{\times}10^{5}$	$2.55{\times}10^{5}$	$6.85{\times}10^{5}$	$7.18{\times}10^{5}$	$8.16{\times}10^{6}$	$1.83{\times}10^{5}$	$3.40{\times}10^{6}$	$7.71{\times}10^{4}$
14	$4.15{\times}10^{5}$	$5.08{\times}10^{5}$	$1.56{\times}10^{6}$	$1.41{\times}10^{6}$	$1.69{\times}10^{7}$	$3.31{\times}10^{5}$	$9.28{\times}10^{6}$	$1.80{\times}10^{5}$
15	$3.58{\times}10^{4}$	$5.79{\times}10^{4}$	$1.03{\times}10^{5}$	$1.58{\times}10^{5}$	$2.83{\times}10^{5}$	$7.66{\times}10^{4}$	$9.82{\times}10^{4}$	$2.77{\times}10^{4}$
16	$4.28{\times}10^{4}$	$6.44{\times}10^{4}$	$1.24{\times}10^{5}$	$1.76{\times}10^{5}$	$5.67{\times}10^{5}$	$8.11{\times}10^{4}$	$1.98{\times}10^{5}$	$2.90{\times}10^{4}$
17	$5.65{\times}10^{5}$	$7.75{\times}10^{4}$	$1.64{\times}10^{5}$	$2.13{\times}10^{5}$	$1.14{\times}10^{6}$	$9.03{\times}10^{4}$	$4.21{\times}10^{5}$	$3.15{\times}10^{4}$
18	$8.34{\times}10^{4}$	$1.04{\times}10^{5}$	$2.44{\times}10^{5}$	$2.89{\times}10^{5}$	$2.28{\times}10^{6}$	$1.09{\times}10^{5}$	$8.96{\times}10^{5}$	$3.68{\times}10^{4}$
19	$1.63{\times}10^{5}$	$2.03{\times}10^{5}$	$5.03{\times}10^{5}$	$5.75{\times}10^{5}$	$5.73{\times}10^{6}$	$1.63{\times}10^{5}$	$2.31{\times}10^{6}$	$5.66{\times}10^{4}$
20	$3.01{\times}10^{5}$	$3.68{\times}10^{5}$	$9.80{\times}10^{5}$	$1.03{\times}10^{6}$	$1.15{\times}10^{7}$	$2.55{\times}10^{5}$	$4.93{\times}10^{6}$	$1.12{\times}10^{5}$
21	$5.77{\times}10^{5}$	$7.04{\times}10^{5}$	$1.83{\times}10^{6}$	$1.66{\times}10^{6}$	$2.33{\times}10^{7}$	$4.46{\times}10^{5}$	$1.28{\times}10^{7}$	$2.49{\times}10^{5}$

Chapter 5

Correlation of ice calibrating clouds

The GPM DPRKa and CloudSat CPR datasets have been further exploited to determine what is the difference in terms of reflectivity probability distribution functions (pdfs) of ice calibrating clouds when sampled at a given distance, Δs. The goal is to find how many calibration points are necessary to calibrate the radar within a certain precision, and how long it takes to collect that number of calibration points. The separation distance, Δs, is derived for each intersection criteria by summing together the time constraint and the effect that the time constraint takes on the clouds:

$$\Delta s = \sqrt{\Delta r^2 + v_{wind}^2 \Delta t^2} \tag{5.1}$$

where Δr and Δt are the distance and the time constraint of the selected criterion and v_{wind} is the mean value of the wind speed moving the calibrating natural targets.

Pairs of 5 km horizontal resolution wide cloud samples separated by Δs (defined in Tab. 3.3 and Eq. 5.1) are extracted from the radar measurements. The data are extracted along the spacecraft track. For GPM, only the five scans around nadir have been used. In Fig. 5.1 is depicted a cloud system with the data separation described above. The ice clouds within black and blue dashed lines are accumulated separately to form two independent PDFs that correspond to samples separated by Δs. This procedure simulates the sampling of two clouds located at a separation distance Δs from each other, acted by two different radars of the same band. Basically the same action that occur in the cross-calibration.

The PDFs obtained above have been cut at the edges to match the refectivity of the ice calibrating clouds chosen for the radar calibration: values from -20 to 25 dBZ and from 15 to 40 dBZ are taken for the W and Ka-band respectively.

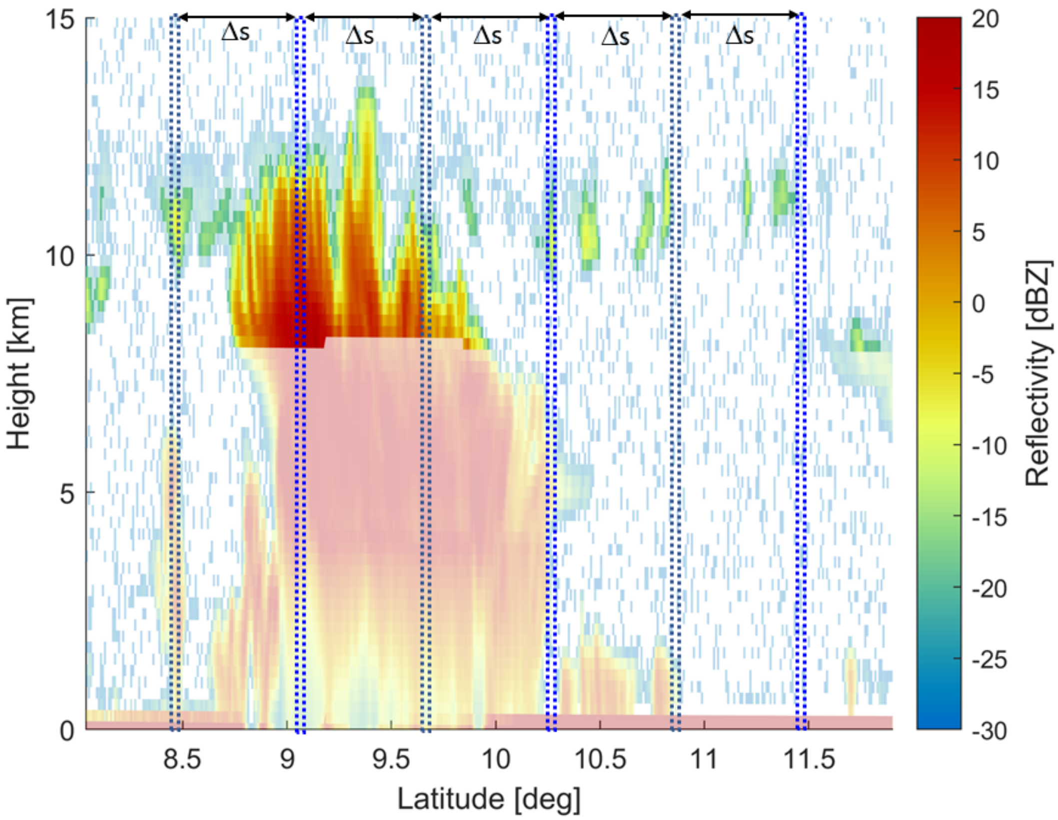

Figure 5.1: Tropical cloud system. The dot lines represent the 5km wide vertical piece of data separated by a distance equal to Δs. Figure submitted in [4].

Examples of those PDFs for both Ka and W-band are shown in Fig. 5.2. The median of the envelope of those PDFs is depicted with a dashed black line. The 5^{th} and 95^{th} percentile is shown as a grey shading.The Z-PDF value decreases with increasing reflectivities values at both Ka and W-band, while the relative noisiness increases at higher Z values, which have low probability to occur. For the W-band PDF (right panel) the effect of a positive bias of 1 and 2 dB is shown by the green and the yellow curve, respectively. Higher is the bias, higher is its curve departure from the median behaviour and a higher number of points of the curve is locate outside of the shaded region.

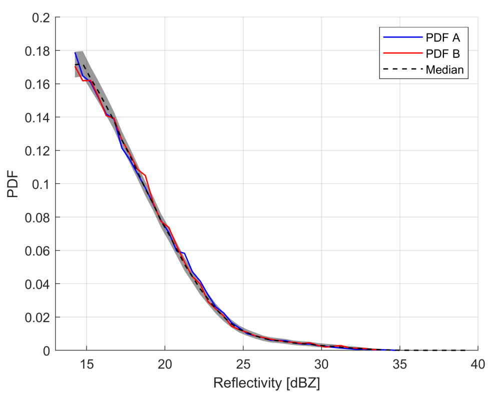

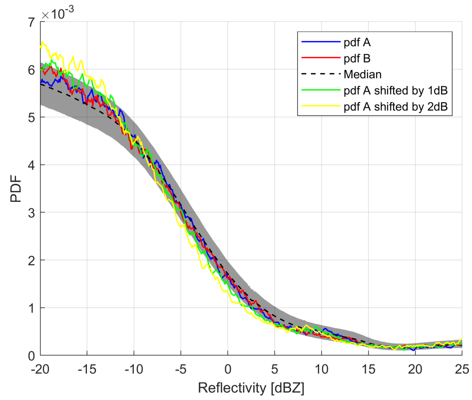

Figure 5.2: Envelope (5-95th percentile) of Z-PDFs for the Ka-band ice calibrating clouds (left panel) and for the W-band ice calibrating clouds (right panel). The black line represents the median PDF while the blue and red curve represent two PDFs randomly selected. Both PDFs are normalised to have the same area. The Ka and W-band PDFs have been built with a number of points of respectively around 5E+04 and 1E+05. For the W-band PDF the effect of a positive bias of 1 and 2 dB is also shown. Figures submitted in [4].

5.1 Jensen-Shannon distance of biased and unbiased reflectivity PDFs

The Jensen-Shannon (J-S) distance is a method of measuring the similarity between two probability distributions functions. The J-S distance between two PDFs is defined as

$$d_{JS} = \sqrt{\frac{\mathcal{D}_{KL}(P,M) + \mathcal{D}_{KL}(Q,M)}{2}} \tag{5.2}$$

where $M = (P+Q)/2$ and $\mathcal{D}_{KL}$ is the Kullback–Leibler divergence defined as:

$$\mathcal{D}_{KL}(P,Q) = \sum_x P(x)\ \log_2 \frac{P(x)}{Q(x)}. \tag{5.3}$$

Once two Z-PDFs of samples separated by Δs are accumulated, the Jensen-Shannon distance between them is computed. In the example illustrated in Fig.5.2, the J-S distance computed between the median PDF (black dashed line) and the blue, red, green and yellow curves is 0.0338, 0.0334, 0.0476, 0.0646, respectively. It can be noticed that, higher bias produces higher J-S distance, and higher J-S distance means that a larger departure from the median PDF is present.

In order to understand what is the behavior of the J-S distance computed between reflectivity PDFs collected by two radars from clouds located at a given separation distance from each other, the previously described procedure is repeated for different sample size and for an ensemble of pairs large enough to generate the distribution function of J-S distances, for any sample size, and for any separation distance. The median value (black continuous line) of J-S distance as a function of the number of calibrating points for the ensamble of pairs of Ka and W-band is shown in Fig. 5.4 for a separation distance equal to 500 and 100 km respectively. It decreases with the increment of number of calibrating points. The 5^{th} and the 95^{th} percentile (black dashed lines) are also shown in the picture and they represent the range of values taken by the J-S distance.

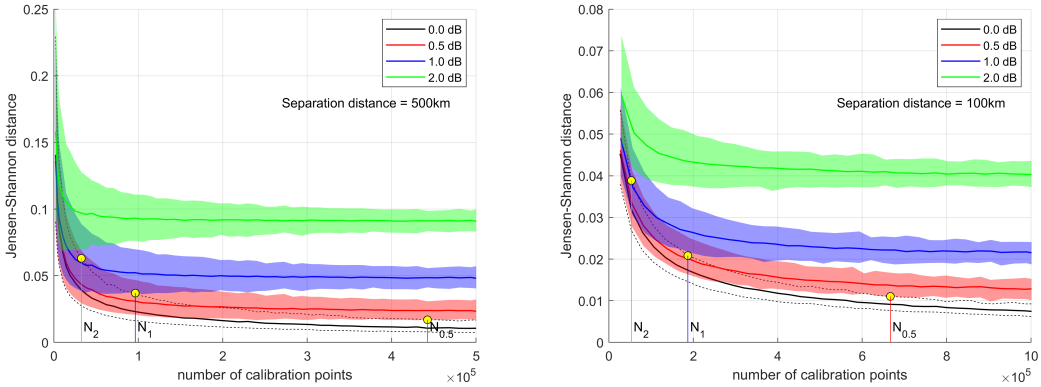

Figure 5.3: Plot of the J-S distances for Ka (left) and W-band (right) Z-PDFs for ice calibrating clouds located at 500 km (left) and 100 km (right) from each other. The black line represent the median distance, while the 5th and the 9th percentile are depicted with the dashed black lines. The coloured lines represent the median distance obtained when shifting one of the two Z-PDFs of the pair of a calibration bias of +0.5, +1.0 and +2.0; the corresponding coloured shadings represent the area between the 5^{th} and the 95^{th} percentile. Figures submitted in [4].

The same procedure is repeated by shifting one of the two Z-PDFs of the pair by a reflectivity bias (e.g 0 dB, ±0.5 dB, ±1.0 dB, ±2.0 dB, ...) to simulate a miscalibration and see what it its effect on the J-S distances. All J-S distances increase with the bias, higher is the magnitude of the bias, higher is the increment in J-S distance, as shown in Fig. 5.3, where positive bias of +0.5, +1.0 and +2.0 dB are considered. Very similar results are obtained when negative bias are applied.

It can be noticed that, for each calibration bias, there is a threshold in terms of number of calibrating points:

- below which, the range of values in the corresponding coloured shadings overlaps the unbiased range of values delimited by the black dashed lines;
- above the threshold, the range of values in the corresponding coloured shadings

is clearly distinct and separated from the unbiased range of values delimited by the black dashed lines.

Therefore, below this threshold, the bias, at which the J-S distances have been generated, cannot be unequivocally identified. Above the threshold, the envelopes are well separated and the miscalibration bias is well defined. In other words, the previously described threshold represents the minimum number of calibration points above which the envelopes of the unbiased and biased J-S distances are clearly distinct.
For the three biases shown in the right panel of Fig. 5.3, the values of that threshold are $N_{0.5}$, N_1 and N_2, where $N_{0.5} > N_1 > N_2$. Let's take, for instance, a separation distance of less than 100 km and 100,000 calibrating point. A 2 dB bias produces J-S distances above 0.038 (which is the distance at the 5th percentile) that are incompatible with the range of values determined by the natural variability of the unbiased envelope between 0.019 and 0.028 (respectively 5^{th} and 95^{th} percentiles, dashed black lines). Instead, a 1 dB bias generate J-S distances between 0.024 and 0.037 and consequently cannot be unequivocally identified. On the other hand, taking a sample larger than $N_1 = 187{,}210$ would guarantee the capability of identifying the a bias of 1 dB. A much higher value ($N_{0.5} = 667{,}700$) is required to identify a miscalibration of 0.5 dB.
Therefore the plots in Fig 5.3 can be used to understand what reflectivity biases are detectable when collecting a certain number of reflectivity measurements (that corresponds to calibration points) located within a certain distance, and consequently, the number of calibration points needed to achieve a calibration accuracy equal to the considered bias. The number of points needed to detect a miscalibration of ± 0.5 dB, ± 1.0 dB, ± 2.0 dB are shown in Tab. 5.1.

The J-S distance as a function of number of calibrating points when varying Δs is shown in Fig. 5.4. The medians are shown as a continuous lines, the 5th and the 95th percentiles are shown for separation distances of 5 km and 1000 km. Higher Δs produces higher J-S distances as expected. In fact, the smaller is the separation distance at which the reflectivities have been aggregated and more those reflectivities are correlated. However, at large Δs, the distance between the median curves becomes smaller and smaller. In fact it can be noticed that, e.g at $\Delta s = 1000$ and 2500 km there is a minimal difference. This property means that, for a calibration purpose, the usage of higher Δs is more effective in order to collect the same number of points in a shorter time.

Table 5.1: Minimum number of calibration points above which the envelopes of the unbiased and biased J-S distances are clearly distinct for each different criteria (or Δs). Positive biases of 0.5, 1 and 2 dB are are reported for both the Ka and W-band. Negative biases are also shown for the W-band. The symbol "–" means a larger number of points than the sample studied is needed.

Band	Ka			W					
	Minimum number of calibration points needed to detect a miscalibration of								
Miscal. [dB] / Δs [km]	0.5	1.0	2.0	-0.5	-1.0	-2.0	0.5	1.0	2.0
25	2.0×10^5	5.2×10^4	1.7×10^4	4.2×10^5	1.1×10^5	3.3×10^4	4.2×10^5	1.3×10^5	3.3×10^4
50	3.0×10^5	7.1×10^4	2.2×10^4	5.8×10^5	1.6×10^5	4.4×10^4	6.8×10^5	1.6×10^5	4.4×10^4
100	3.6×10^5	8.1×10^4	2.9×10^4	8.8×10^5	1.9×10^5	5.3×10^4	6.9×10^5	1.9×10^5	5.3×10^4
200	3.8×10^5	8.8×10^4	2.9×10^4	7.1×10^5	1.8×10^5	5.4×10^4	7.2×10^5	2.0×10^5	5.4×10^4
500	4.4×10^5	9.6×10^4	3.3×10^4	8.8×10^5	2.8×10^5	5.5×10^4	1.2×10^6	2.8×10^5	7.1×10^4
1000	5.0×10^5	1.0×10^5	2.9×10^4	–	2.8×10^5	6.1×10^4	–	14.4×10^5	8.8×10^4
2000	6.1×10^5	1.2×10^5	2.9×10^4	–	–	1.1×10^5	–	–	8.1×10^4

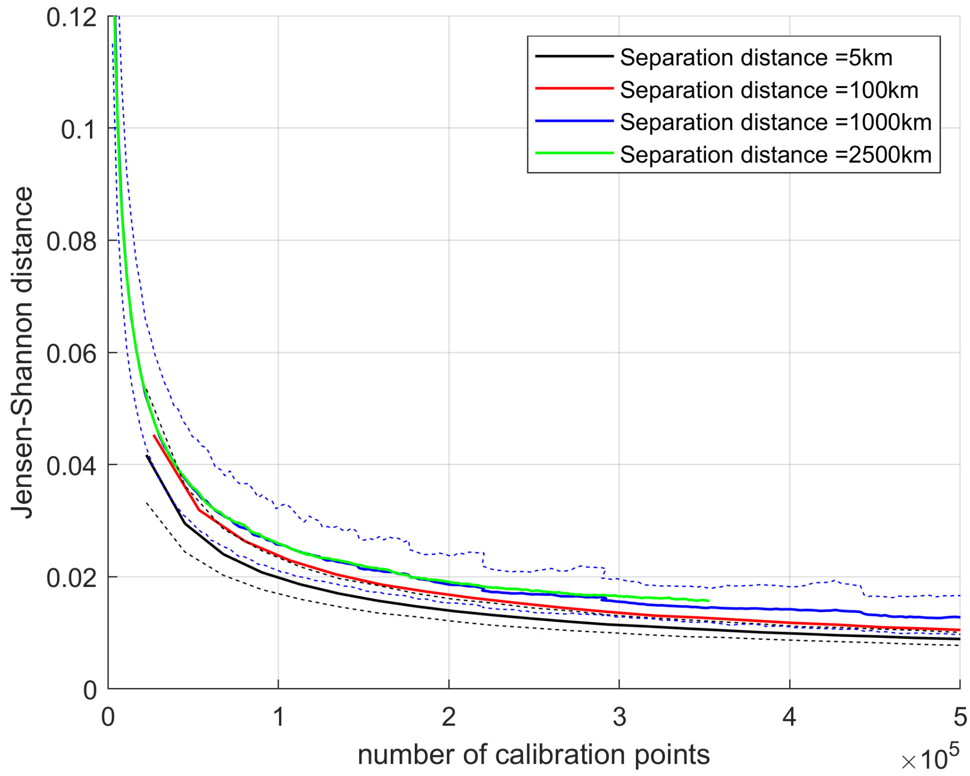

Figure 5.4: How the separation distance affect the Jensen-Shannon distance as a function of number of points and for the W-band calibrating targets. The continuous coloured lines represent the median of the J-S distance for different separation distances, while the black and blue dashed lines correspond to the 5^{th} and 95^{th} percentiles for the 5 and 1000 km separation distances, respectively. Figure submitted in [4].

Chapter 6

Results of cross-calibration performance

The number of calibrating points obtained in Chapter 5 and the result of the calibration target correlation analysis carried out in Chapter 4 are merged to determine what is the achievable calibration accuracy that can be established in a given time period (e.g. weekly), in order to assess what is the more optimal intersection criterion among those listed in Tab. 3.3. The minimum number of calibration points needed to achieve a certain calibration accuracy (reported in Tab. 5.1) are transformed in number of days needed to collect that number of calibration points, reported in Tab. 6.1. This is performed using the mean number of calibration points accumulated per week by each radar-pair configuration, summarized in Tab. 4.1. A conservative approach has been used and, for each of those configuration, the lowest number of the two columns have been used (e.g for the Wiver-AOS1 configuration, the number of points sampled by AOS1 have been considered).

Generally, criteria with large Δs perform better. The high number of coincidences obtained with those criteria overcomes the lower correlation of cloud Z-PDFs. Thanks to the large swath of GPM KaPR and Tomorrow.io radar, the cross calibration of Tomorrow.io can be achieve within 1 dB on an average of few days, less than two days are needed if we consider criterion #14 and #21. It is a very good result for the Tomorrow.io constellation. Furthermore, a better calibration with an accuracy of 0.5 dB seems viable within a period of few days for the inclined Tomorrow.io and within a week for the polar Tomorrow.io.

The cross-calibration of Wivern with the AOS radars can be achieved with an accuracy better than 1 dB within less than 7 days for AOS1, and less than 10 days for AOS2 (both with criterion #21). A calibration within 2 dB can be realized more quickly: within two and three days for AOS1 and AOS2 respectively).

GPM and Tomorrow.io have a better cross-calibration performance than Wivern

Table 6.1: Mean number of days required to achieve a calibration accuracy for the different criteria listed in Tab. 3.3 and for the four satellite configurations analysed in this study. The symbol – means that the given level of accuracy cannot be achieved.

Configuration	Tomorrow.io1-GPM			Tomorrow.io2-GPM			Wivern-AOS1			Wivern-AOS2		
	Mean number of days required to achieve a calibration accuracy better than											
Miscal. [dB] / Crit. #	0.5	1.0	2.0	0.5	1.0	2.0	0.5	1.0	2.0	0.5	1.0	2.0
1	107.0	27.4	9.1	39.8	10.2	3.4	108	32	8.4	311	92.3	24.3
2	133.0	31.5	9.8	49.3	11.7	3.6	151	37.8	12.6	441	110	36.8
3	121.0	27.2	9.8	44.7	10.0	3.6	142	39.9	1.14	426	120	34.2
4	85.7	20.0	6.5	31.1	7.3	2.4	124	35.7	9.5	385	111	29.7
5	50.5	11.0	3.7	17.2	3.7	1.3	140	31.8	7.5	436	99.4	23.4
6	29.9	6.1	1.7	9.5	1.9	0.5	–	21.8	6.2	–	52.7	14.9
7	17.8	3.4	0.8	4.6	0.9	0.2	–	12.4	3.0	–	23.9	5.7
8	57.7	14.8	4.9	20.2	5.2	1.7	55.3	16.4	4.3	160	47.4	12.5
9	71.6	17.0	5.3	25.0	5.9	1.8	77.6	19.4	6.5	227	56.8	19.0
10	65.3	14.7	5.3	22.7	5.1	1.8	73.6	20.7	5.9	220	61.8	17.7
11	46.2	10.8	3.5	15.9	3.7	1.2	64.8	18.7	5.0	200	57.6	15.4
12	27.4	6.0	2.0	8.9	1.9	0.7	74.4	17.0	4.0	227	51.7	12.2
13	16.7	3.4	1.0	5.1	1.0	0.3	–	11.9	3.4	–	28.3	8.1
14	10.3	2.0	0.5	2.8	0.5	0.1	–	7.18	1.7	–	13.2	3.2
15	39.4	10.1	3.4	13.7	3.5	1.2	38.8	11.5	3.0	107	31.8	8.4
16	49.0	11.7	3.6	17.0	3.5	1.3	54.5	13.6	4.5	152	38.1	12.7
17	44.8	10.1	3.6	15.4	3.5	1.2	51.7	14.5	4.1	148	41.5	11.9
18	31.7	7.4	2.4	10.8	2.5	0.8	45.6	13.2	3.5	135	38.8	10.4
19	19.0	4.1	1.4	6.2	1.3	0.5	52.6	12.0	2.8	152	34.6	8.2
20	11.6	2.4	0.7	3.6	0.7	0.2	–	8.54	2.4	–	19.6	5.6
21	7.4	1.4	0.4	2.4	0.5	0.1	–	5.32	1.3	–	9.51	2.3

and AOS, thanks to the larger swath of GPM and Tomorrow.io radars. In fact, the lack of scanning by the AOS radars causes the number of calibration points collected to be very low if compared to those sampled by Tomorrow.io, GPM, and Wivern. This limits the cross-calibration performance of Wivern.

These are mean results base on annual orbital intersections and on annual climatology of clouds. There may be particular conditions where the lacks of orbital intersections or lack of ice calibrating clouds are present. Therefore, in that cases, longer periods of time are needed to achieve radar calibration. However, as shown in Fig. 6.1, at the criterion #21 (the one that gives best results), the variability on a weekly basis of the orbital intersections are very small. In particular, the weekly variability for Wivern is insignificant with both AOS1 and AOS2. Instead, it is higher for Tomorrow.io1 radar with a cycle that exceeds one year, and it is the largest for the Tomorrow.io2-GPM radar pair.

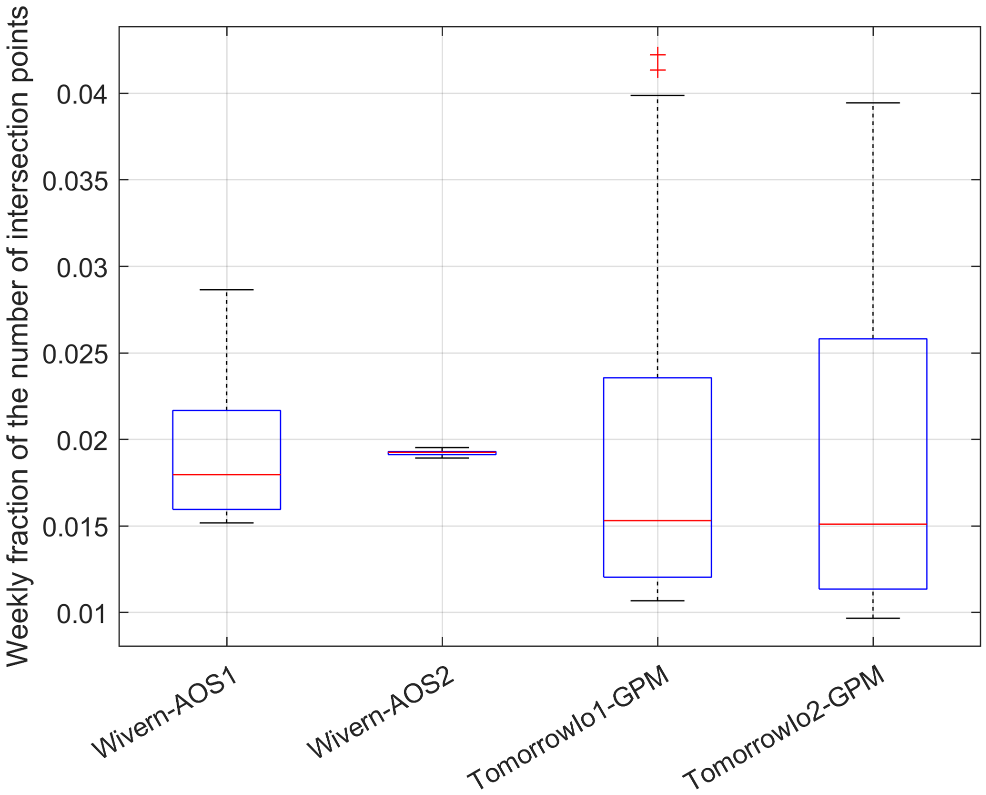

Figure 6.1: Whisker plot with the weekly fraction of the year calibration points for the 52 weeks of the year for the four satellite configurations considered in this study. Figure submitted in [4].

Since it seems that higher is the Δt and the Δr and higher is the calibration performance, might be interesting to understand if an absolute calibration based on the curves of the global climatology of ice clouds Z-PDFs are feasible. With the help of GPM KaPR and CloudSat CPR datasets the following steps have been followed:

- a global climatology Z-PDF (PDF_1) covering 4 years of data is generated;
- a separate Z-PDF has been produced for each day of the dataset (PDF_j) and J-S distance between PDF_1 and PDF_j have been computed for a weekly and monthly aggregation intervals;
- each PDF_j is shifted by ±0.5, ±1 and ±2 dB and the J-S distances between

PDF_1 and the six shifted PDF_j are computed;

- time series of the seven J-S distances computed between PDF_1 and unshifted and shifted PDF_j are generated and compared.

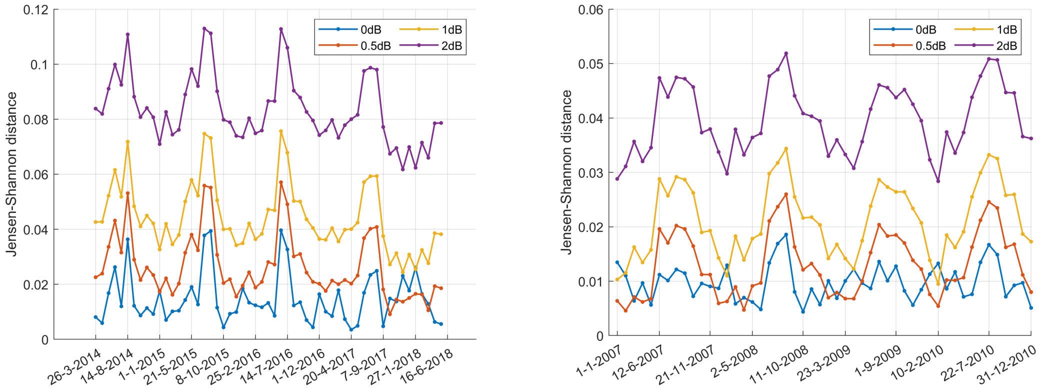

Figure 6.2: Time series of the J-S distances computed between monthly accumulated Z-PDFs and four years of Ka (left) and W-band (right) climatology. Figures submitted in [4].

Results accumulated at a monthly scales are illustrated in Fig. 6.2 for the Ka (left) and W-band (right). It shows that calibration with respect to the global climatology is attainable within 1 dB at a such temporal scale. Also, a weekly calibration is feasible within 2 dB.

Chapter 7

Summary and conclusions

This dissertation presents a methodology for calibrating conically scanning spaceborne radars by using cross-calibration with reference to other spaceborne radars working at the same band and orbiting around Earth in the same period of time. Different examples have been discussed in the thesis:

- the calibration of Tomorrow.io Ka-band radars with GPM KaPR used as reference;
- the calibration of Wivern W-band radar with NASA AOS mission radars used as calibrators.

Ice clouds at low temperature are used as calibration targets due to their low predisposition in causing signal attenuation.

Radar antenna boresight positions have been propagated on the basis of the satellite orbits. Radars' ground-track intersections have been computed for different intersection criteria defined by cross-overs withing a certain time intervals and certain distance and their distribution over the globe has been determined.

Then, the climatology of Ka and W-band ice calibrating clouds has been studied using the GPM KaPR and CloudSat CPR dataset, respectively. The global distribution of such clouds and their frequency have been obtained. The number and the global distribution of the calibration points have been retrieved by multiplying the ground-track intersections by the climatology of ice calibrating clouds.

The GPM and CloudSat datasets have been further exploited to study the similarity between reflectivity distribution functions of ice calibrating clouds at different separation distances in order to find what is the optimal intersection criterion (listed in Tab 3.3) that maximize the calibration accuracy and minimize the time needed to achieve that. Higher is the distance criterion and higher is the number of calibration points collected. However at higher separation distances the

statistical correlation of calibrating clouds reflectivities is lower. A trade-off between having a high number of calibrating points and having a reasonable correlated ice clouds properties is needed.
The result of all the analysis for the Ka-band climatology are a courtesy of Kamil Mroz.

The results of this study demonstrate the effectiveness of this methodology in calibrate within 1 dB a Ka (like Tomorrow.io) and a W-band (like Wivern) conically scanning radar every few days and in a week, respectively. These levels of uncertainty meets the mission requirements and the standard currently achieved with absolute calibration accuracy. The better performances obtained for Tomorrow.io are caused by a better suited shape of the Z-PDF to perform cross-calibration, and by the higher number of intersection points collected by the combination of the scanning pattern of Tomorrow.io radars and GPM .

The global climatology reflectivity PDF (black continuous lines in Fig 5.2) can be used as an absolute reference to perform the calibration, and the J-S distance could be computed with respect to such PDF. This would eliminate the necessity of having intersection points. However, how the natural variability originated by the regional, diurnal and seasonal cycles affects the PDF itself is not known. More research in this area and more global observations of the ice cloud cycles need to be done.

Calibration of radar reflectivity is very important for producing a correct quantitative estimation of the hydrometeor mass contents and mass fluxes, which are the main and most important products in the cloud and precipitation radar missions. The methodology described in this dissertation can be used to estimate the cross-calibration accuracy obtainable with orbital cross-overs and will be usable for the calibration of the Ka-band Tomorrow.io and the INCUS train [23] radars, which will be lauched from the end of 2013 and in 2017, respectively.

Bibliography

[1] Roger R. Bate, Donald D. Mueller, and Jerry E. White. *Fundamentals of Astrodynamics*. Dover Publications, 1971 (cit. on pp. 14, 16, 17).

[2] A. Battaglia, R. Dhillon, and A. Illingworth. «Doppler W-band polarization diversity space-borne radar simulator for wind studies». In: *Atmospheric Measurement Techniques* 11.11 (2018), pp. 5965–5979. DOI: `10.5194/amt-11-5965-2018`. URL: `https://amt.copernicus.org/articles/11/5965/2018/` (cit. on p. 2).

[3] A. Battaglia, P. Martire, E. Caubet, L. Phalippou, F. Stesina, P. Kollias, and A. Illingworth. «Observation error analysis for the WInd VElocity Radar Nephoscope W-band Doppler conically scanning spaceborne radar via end-to-end simulations». In: *Atmospheric Measurement Techniques* 15.9 (2022), pp. 3011–3030. DOI: `10.5194/amt-15-3011-2022`. URL: `https://amt.copernicus.org/articles/15/3011/2022/` (cit. on pp. 2, 3).

[4] A. Battaglia, F. E. Scarsi, K. Mroz, and A. Illingworth. «Cross-calibration of millimeter conically scanning spaceborne radars». In: *Atmospheric Measurement Techniques* (2022). submitted in July 2022 (cit. on pp. 3, 9, 26, 28, 29, 35, 37–40, 45–47, 50, 53, 54).

[5] A. Battaglia, M. Wolde, L. P. D'Adderio, C. Nguyen, F. Fois, A. Illingworth, and R. Midthassel. «Characterization of Surface Radar Cross Sections at W-Band at Moderate Incidence Angles». In: 55.7 (2017). 10.1109/TGRS.2017.2682423, pp. 3846–3859 (cit. on p. 8).

[6] Alessandro Battaglia, Pavlos Kollias, Ranvir Dhillon, Richard Roy, Simone Tanelli, Katia Lamer, Mircea Grecu, Matthew Lebsock, Daniel Watters, Kamil Mroz, Gerald Heymsfield, Lihua Li, and Kinji Furukawa. «Spaceborne Cloud and Precipitation Radars: Status, Challenges, and Ways Forward». In: *Reviews of Geophysics* 58.3 (2020). e2019RG000686 10.1029/2019RG000686, e2019RG000686. DOI: `10.1029/2019RG000686`. eprint: `https://agupubs.onlinelibrary.wiley.com/doi/pdf/10.1029/2019RG000686`. URL: `https://agupubs.onlinelibrary.wiley.com/doi/abs/10.1029/2019RG000686` (cit. on pp. 1, 2, 5).

[7] David R. Brunfeldt and Fawwaz T. Ulaby. «Active Reflector for Radar Calibration». In: *IEEE Transactions on Geoscience and Remote Sensing* GE-22.2 (1984), pp. 165–169. DOI: 10.1109/TGRS.1984.350610 (cit. on p. 8).

[8] Michel Capderou. *Handbook of Satellite Orbits*. Springer International Publishing, 2014 (cit. on p. 18).

[9] Howard D. Curtis. *Orbital Mechanics for Engineering Students*. Butterworth-Heinemann, 2019 (cit. on pp. 15, 16).

[10] D.M. Endres and J.E. Schindelin. «A new metric for probability distributions». In: *IEEE Transactions on Information Theory* 49.7 (2003), pp. 1858–1860. DOI: 10.1109/TIT.2003.813506 (cit. on p. 10).

[11] Frédéric Fabry. *Radar Meteorology: Principles and Practice*. Cambridge University Press, 2015. DOI: 10.1017/CBO9781107707405 (cit. on pp. 2, 4, 6).

[12] Yulan Hong and Guosheng Liu. «The Characteristics of Ice Cloud Properties Derived from CloudSat and CALIPSO Measurements». In: *Journal of Climate* 28.9 (2015), pp. 3880–3901. DOI: 10.1175/JCLI-D-14-00666.1. URL: https://journals.ametsoc.org/view/journals/clim/28/9/jcli-d-14-00666.1.xml (cit. on p. 37).

[13] A.J. Illingworth, A. Battaglia, J. Bradford, M. Forsythe, P. Joe, P. Kollias, K. Lean, M. Lori, J.F. Mahfouf, S. Melo, R. Midthassel, Y. Munro, J. Nicol, R. Potthast, M. Rennie, T.H.M. Stein, S. Tanelli, F. Tridon, C.J. Walden, and M. Wolde. «WIVERN: A New Satellite Concept to Provide Global In-Cloud Winds, Precipitation, and Cloud Properties». In: *Bulletin of the American Meteorological Society* 99.8 (Aug. 2018), pp. 1669–1687. DOI: 10.1175/BAMS-D-16-0047.1 (cit. on pp. 1, 2, 33).

[14] A.J. Illingworth, A. Battaglia, J. Delanoe, G. Halloran, P. Kollias, S. Laroche, J.F. Mahfouf, R. Potthast, M. Rennie, C.J. Walden, and M. Wolde. *WIVERN: A WInd VElocity Radar Nephoscope for observing global winds, clouds and precipitation*. A proposal submitted to ESA in response to the Call for Earth Explorer-11 Mission Ideas. Dec. 2020 (cit. on pp. 2, 12).

[15] Hyung-Chul Lim, Hyochoong Bang, and Sangjong Lee. «Adaptive Backstepping Control for Satellite Formation Flying with Mass Uncertainty». In: *Journal of Astronomy and Space Sciences* 23 (Dec. 2006), pp. 405–414. DOI: 10.5140/JASS.2006.23.4.405 (cit. on p. 16).

[16] Takeshi Masaki, Toshio Iguchi, Kaya Kanemaru, Kinji Furukawa, Naofumi Yoshida, Takuji Kubota, and Riko Oki. «Calibration of the Dual-Frequency Precipitation Radar Onboard the Global Precipitation Measurement Core Observatory». In: *IEEE Transactions on Geoscience and Remote Sensing* 60 (2022), pp. 1–16. DOI: 10.1109/TGRS.2020.3039978 (cit. on pp. 2, 7).

[17] Robert Meneghini and Toshiaki Kozu. *Spaceborne weather radar*. Artech House, 1990 (cit. on p. 2).

[18] NASA. *GPM Core Observatory*. URL: `https://gpm.nasa.gov/missions/GPM/core-observatory` (cit. on p. 11).

[19] NASA. *GPM Dual-frequency Precipitation Radar*. URL: `https://gpm.nasa.gov/missions/GPM/DPR` (cit. on p. 11).

[20] World Meteorological Organization. *WMO strategic plan 2020–2023*. 2019 (cit. on p. 1).

[21] World Climate Research Program. *WCRP Grand Challenges*. URL: `https://www.wcrp-climate.org/grand-challenges/grand-challenges-overview` (cit. on p. 1).

[22] CloudSat project. *Level 2 GEOPROF Product Process Description and Interface Control Document*. URL: `https://www.cloudsat.cira.colostate.edu/` (cit. on p. 33).

[23] Graeme L. Stephens, Susan C. van den Heever, Ziad S. Haddad, Derek J. Posselt, Rachel L. Storer, Leah D. Grant, Ousmane O. Sy, T. Narayana Rao, Simone Tanelli, and Eva Peral. «A Distributed Small Satellite Approach for Measuring Convective Transports in the Earth's Atmosphere». In: *IEEE Transactions on Geoscience and Remote Sensing* 58.1 (2020), pp. 4–13. DOI: `10.1109/TGRS.2019.2918090` (cit. on p. 56).

[24] Simone Tanelli, Stephen L. Durden, Eastwood Im, Kyung S. Pak, Dale G. Reinke, Philip Partain, John M. Haynes, and Roger T. Marchand. «CloudSat's Cloud Profiling Radar After Two Years in Orbit: Performance, Calibration, and Processing». In: *IEEE Transactions on Geoscience and Remote Sensing* 46.11 (2008), pp. 3560–3573. DOI: `10.1109/TGRS.2008.2002030` (cit. on pp. 2, 7, 8).

[25] M. Wolde, A. Battaglia, C. Nguyen, A. L. Pazmany, and A. Illingworth. «Implementation of polarization diversity pulse-pair technique using airborne W-band radar». In: 12.1 (2019), pp. 253–269. DOI: `10.5194/amt-12-253-2019`. URL: `https://www.atmos-meas-tech.net/12/253/2019/` (cit. on p. 8).